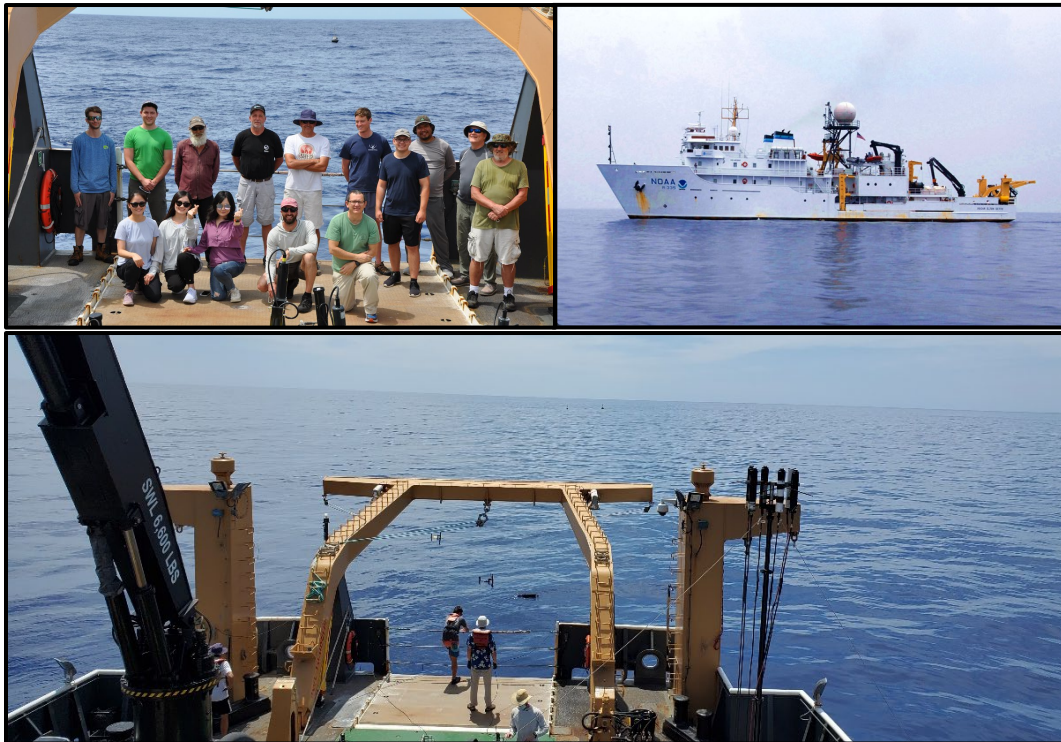**NOAA Technical Report NESDIS 160**

Report for Dedicated JPSS VIIRS Ocean Color Calibration/Validation Cruise: Hawaii in March 2022

US DEPARTMENT OF COMMERCE
National Oceanic and Atmospheric Administration
National Environmental Satellite, Data, and Information Service
Washington, D.C.
February 2024

Previous NESDIS Technical Reports on the Dedicated JPSS-VIIRS-Ocean Color Calibration/Validation Cruise Series:

Report #146	**November 2014**	**https://doi.org/10.7289/V52B8W0Z**
Report #148	**December 2015**	**https://doi.org/10.7289/V5/TR-NESDIS-148**
Report #151	**October 2016**	**https://doi.org/10.7289/V5/TR-NESDIS-151**
Report #152	**May 2018**	**https://doi.org/10.25923/scyb-qf42**
Report #154	**September 2019**	**https://doi.org/10.25923/p9de-yw97**
Report #157	**October 2022**	**https://doi.org/10.25923/x2q6-9418**

[*] Cover image (clockwise from top left): cruise participants; NOAA Ship *Oscar Elton Sette*; deployment of floating radiometers by the science crew.

Report for Dedicated JPSS VIIRS Ocean Color Calibration/Validation Cruise:
Hawaii in March 2022

Editor

Jianwei Wei[1,2*]
[1]NOAA/NESDIS Center for Satellite Applications and Research, College Park, MD 20740;
[2]Global Science & Technology, Inc., Greenbelt, MD 20770
[*] Corresponding author: jianwei.wei@noaa.gov

Contributing authors:

Michael Ondrusek[1*], Menghua Wang[1], Eric Stengel[1], and Charles Kovach[1,2]
[1]NOAA/NESDIS Center for Satellite Applications and Research, College Park, MD 20740;
[2]Global Science & Technology, Inc., Greenbelt, MD 20770
[*]michael.ondrusek@noaa.gov

And (in alphabetical order by group lead's last name):

Alex Gilerson[*], Eder Herrera, and Mateusz Malinowski
City College of the City University of New York, New York, NY 10031
[*]gilerson@ccny.cuny.edu

Joaquim I. Goes[*], Jinghui Wu, and Helga do Rosario Gomes
Lamont Doherty Earth Observatory at Columbia University, NY 10964
[*]jig@ldeo.columbia.edu

Chuanmin Hu[*], Jennifer Cannizzaro, David English, Jing Shi, and Yao Yao
College of Marine Science, University of South Florida, St. Petersburg, FL 33701
[*]huc@usf.edu

Sherwin Ladner[*]
Naval Research laboratory, Stennis Space Center, MS 39529
[*]sherwin.ladner@nrlssc.navy.mil

Antonio Mannino[1*], Joaquín E. Chaves [1,2], Declan P. Farr[3], Scott A. Freeman[1,2], and Harrison D. Smith[1,2]
[1]NASA Goddard Space Flight Center, Greenbelt, MD 20771; [2]Science Systems & Applications, Inc., Lanham, MD 20706; [3]US EPA Region 10 Alaska Operations Office, Anchorage, AK 99513
[*]antonio.mannino-1@nasa.gov

Nick Tufillaro[1*], Alexander Bailess[1], Adam Belmonte[1], Andrew Barnard[1], Jing Tan[2], and Robert Frouin[2]
[1]College of Earth, Ocean, and Atmospheric Sciences, Oregon State University, Corvallis, OR 97331
[2]Scripps Institution of Oceanography, University of California San Diego, La Jolla, CA 92093-0230
[*]nbt@coas.oregonstate.edu

Washington, D. C.
February 2024

Table of contents

List of figures

iii

List of tables

Preface

The Ocean Color Science Team at the National Oceanic and Atmospheric Administration (NOAA) Center for Satellite Applications and Research (STAR) is dedicated to the "end-to-end" production of high-quality, "fit for purpose", remotely sensed ocean color products that are required and expected by all NOAA line offices, as well as by external (both applied and research) users. In addition to serving internal needs, NOAA has a role in supporting the international ocean color community and has an active membership in the International Ocean-Colour Coordinating Group (IOCCG). The IOCCG brings attention to the importance of in situ observations for algorithm calibration and validation (Cal/Val) throughout satellite mission lifetimes. NOAA's contributions to in situ satellite Cal/Val are appreciated by the international ocean color community, as well as science and research communities.

Supported by the Joint Polar Satellite System (JPSS) program, the NOAA Ocean Color Science Team has coordinated the ocean color Cal/Val field campaign since 2014 with NOAA, NASA, Navy, universities, and other organizations. The Hawaii cruise in 2022 marked the seventh field cruise. The objective was to conduct field measurements that can be used to construct satellite and in situ matchups and to assess the uncertainties of in situ measurements, including those at the Marine Optical BuoY (MOBY). The matchup data will be used to validate the Visible Infrared Imaging Radiometer Suite (VIIRS) observations from the Suomi National Polar-orbiting Partnership (SNPP), NOAA-20, and NOAA-21 satellites, which are the primary sources for NOAA operational remotely sensed ocean color data products. In fact, MOBY in situ measurements have served as critical data for the on-orbit vicarious calibration of all global satellite ocean color sensors since 1997. The in situ Cal/Val efforts are essential for maintaining the integrity of NOAA's satellite ocean color data products, which undergo calibration changes in orbit, and for extending the applicability of synoptic water quality data products. In addition, the in situ ocean color data from the Cal/Val campaign can support various international ocean color missions, e.g., the Ocean and Land Colour Instrument (OLCI) on the Sentinel-3 series, the Second-Generation Global Imager (SGLI) on the Global Change Observation Mission-Climate (GCOM-C) satellite, etc. Through the NOAA mission of science, service, and stewardship, and in collaboration with the international ocean community, we strive to provide ocean satellite data products that improve our understanding of global ocean and inland water optical, biological, and biogeochemical properties, which support for research and applications to benefit society.

Menghua Wang, PhD
Chief, Marine Ecosystems & Coastal Branch; VIIRS Ocean Color Cal/Val Team Lead

Paul DiGiacomo, PhD
Chief, Satellite Oceanography & Climatology Division (SOCD), NOAA/STAR

(This page is intentionally left blank)

Abstract

The primary goal of the calibration and validation (Cal/Val) cruise was to conduct coincident matchup measurements to validate VIIRS ocean color data products in clear oceanic waters around the Hawaiian Islands. The secondary goal was to collect measurements for uncertainty evaluations with the Marine Optical Buoy (MOBY) systems. The old, currently operational MOBY instruments are located off Lanai Island. A new MOBY system with a refreshed design was moored about seven nautical miles south of the old MOBY. Most field stations were distributed around the two MOBY sites. The field team, consisting of 15 investigators, also had an opportunity to visit the Hawaii Ocean Time-series (HOT) station north of the Kauai. The NOAA Ship *Oscar Elton Sette* departed from Honolulu on March 7 and returned to port on March 18, 2022, after completing measurements at 23 stations. Various apparent optical properties (AOPs), inherent optical properties (IOPs), and biological and biogeochemical properties were obtained through either in situ measurements or water sample analyses. This document describes the field efforts and achievements of individual teams. Only preliminary results are included in the technical report, while comprehensive analyses and data compilation are underway.

1. Introduction

Calibration and validation (Cal/Val) of satellite ocean color observations are indispensable elements for an Earth observation (EO) mission. The space-borne ocean color sensor measures the total radiance at an altitude of usually hundreds of miles above the ground. It receives a relatively small amount of radiance emerging from the waters and a significant contribution from the atmosphere. As the atmospheric radiance dominates that over water's, minor errors in the measured total radiance at the top-of-atmosphere (TOA) can cause significant uncertainties in derived water-leaving radiance ($L_w(\lambda)$). To overcome this problem, frequent vicarious calibration is performed for the satellite ocean color instruments and these are conventionally conducted with in situ high-quality optical measurements (Wang et al., 2016; Werdell et al., 2007; Zibordi et al., 2015). To derive the water-leaving radiance from the total radiance, one has to estimate the scattering and absorption properties of various gases, water molecules, and aerosols in the atmosphere and the water surface reflection through an atmospheric correction (AC) procedure (Gordon and Wang, 1994; IOCCG, 2010; Wang, 2007). Any uncertainty incurred in the above steps will propagate to the primary ocean color product of remote sensing reflectance ($R_{rs}(\lambda)$) or normalized water-leaving radiance ($nL_w(\lambda)$) and eventually to high-level ocean color products of chlorophyll-a (Chl-a) concentration, diffuse attenuation coefficient at the wavelength of 490 nm ($K_d(490)$), diffuse attenuation coefficient $K_d(PAR)$ at the domain of the photosynthetically available radiation (PAR) (Lee, 2009; Wei and Lee, 2013), suspended particulate matter (SPM) (Wei et al., 2021a), primary production (Wu et al., 2022), etc. Thus it is also of high priority to validate the satellite optical and bio-optical products to gain confidence for the appropriate interpretation of the temporal and spatial trends revealed by satellite observations.

Satellite Cal/Val exercises are conventionally pursued through direct comparison of satellite products to in situ measurements measured beneath the satellite overpass. The in situ measurements can be collected from ship-borne campaigns (Nalli et al., 2022; Wei et al., 2022b), optical buoys such as the Marine Optical BuoY (MOBY) (Clark et al., 2003; Perez et al., 2022), or other marine observatories such as the AErosol RObotic NETwork-Ocean Color (AERONET-OC) (Harmel et al., 2011; Lawson et al., 2019; Zibordi et al., 2009). Satellite products of $R_{rs}(\lambda)$, $nL_w(\lambda)$, and Chl-a are among the frequently examined parameters. Investigations of other products are dependent on the availability of measurements, such as $K_d(\lambda)$ (Wang et al., 2009), light absorption coefficient by phytoplankton ($a_{ph}(\lambda)$), and backscatter coefficient of particles ($b_{bp}(\lambda)$) (Lee et al., 2002; Shi and Wang, 2019). In coastal regions, studies show that relatively small uncertainties can be expected for $R_{rs}(\lambda)$ and $nL_w(\lambda)$ in green bands (Mélin et al., 2011; Qin et al., 2017; Wei et al., 2022b; Wei et al., 2020). However, they can be biased low in short blue bands due to insufficient atmospheric correction (Wang and Jiang, 2018; Wei et al., 2020). In comparison, the satellite $R_{rs}(\lambda)$ data in clear oceanic waters appear more accurate than in coastal waters (Wei et al., 2016). Likewise, the satellite Chl-a products are often susceptible to more considerable uncertainties in coastal regions but relatively small in open oceans (Moore et al., 2009). Note that the matchup data for validation are mostly limited to coastal regions due to logistic requirements.

The Visible Infrared Imaging Radiometer Suite (VIIRS) series is the state-of-the-art ocean color instrument that currently flies onboard the Suomi National Polar-orbiting Partnership (SNPP) (2011–present), NOAA-20 (2017–present), and NOAA-21 (2022–present) satellites, respectively. The VIIRS sensors collect visible, near-infrared (NIR), and shortwave infrared (SWIR) data over the global land, atmosphere, cryosphere, and oceans. For the development of ocean color

Environmental Data Records (EDRs) over global waters, it is critical to maintain timely in situ sampling for validation over various regions of interest and in a continuous manner. Prior to this cruise, six cruises were completed by the Ocean Color Cal/Val Team from 2014 to 2021, expanding from the Mid-Atlantic Bight, the South Atlantic Bight, to the Gulf of Mexico (Ondrusek et al., 2015, 2016; Ondrusek et al., 2017; Ondrusek et al., 2019; Ondrusek et al., 2021; Ondrusek et al., 2022). Primary results after establishing ~100 matchups indicated that VIIRS/SNPP $R_{rs}(\lambda)$ products are subjected to an absolute percentage difference of 43%, 30%, 21%, 17%, and 30% for 410, 443, 486, 551, and 671 nm, respectively (Wei et al., 2022b).

The NOAA Office of Marine and Aviation Operations (OMAO) allocated ship time (SE22-01) for the 2022 cruise with the NOAA Ship *Oscar Elton Sette* (Hull number R335). As before, one primary objective of the cruise is to collect high-quality in situ apparent optical properties (AOPs), inherent optical properties (IOPs), and related biological/biogeochemical data to validate VIIRS ocean color radiometry and higher-level products in open oceans. The second goal is to assess the measurement uncertainties of the MOBY systems (MOBY-old and MOBY-refresh) by comparing them with in situ radiometric observations. Third, we aim to evaluate the measurement uncertainties of in situ deployments. In the following report, we present the cruise contributions of each participating team, with an overarching goal of informing the science community and the management of the preliminary accomplishments from this Cal/Val cruise. Note that all results enclosed in this report are preliminary. Interested readers are encouraged to reach out for the availability of field measurements.

2. Environmental conditions

The North Pacific Subtropical Gyre (NPSG) is the largest ocean ecosystem. It is defined by the North Pacific Current to the north, the edge of the offshore California Current system to the east, the North Equatorial Current to the south, and the offshore edge of the Kuroshio Current to the west. The NPSG is characterized by high sea surface temperature (SST), low nitrate concentration, and extremely low standing stocks of living organisms. The resulting phytoplankton productivity remains low all year long with seasonal variability (Karl et al., 2021). The optical water types are dominantly Class 1 and Class 2, with Chl-a varying between ~0.02–0.2 mg m^{-3} in surface waters (Wei et al., 2022a).

Our investigation area is located around the major islands of Hawaii in the central Pacific Ocean (Figure 1). The water depths are generally over 4000 m. The mountains in Maui are over 3000 m above sea level, and the mountains in the Island of Hawaii (Mauna Loa and Mauna Kea) are even higher (> 4000 m). These islands have a substantial influence on regional oceanic circulations. The prevailing northeasterly trade winds and the spatial extent of the island chain create characteristic and relatively steady forcing of the oceans (Calil et al., 2008). Mesoscale eddies typically develop and persist for weeks to several months to the west of the lee of the island chain. Reports have shown significant consequences of the mesoscale eddies on nutrient-phytoplankton dynamics, community structure, and particle exports (Brown et al., 2008; Dickey et al., 2008; Rii et al., 2008). Figure 2 shows an example of Chl-a, $K_d(490)$, PAR, and $R_{rs}(551)$.
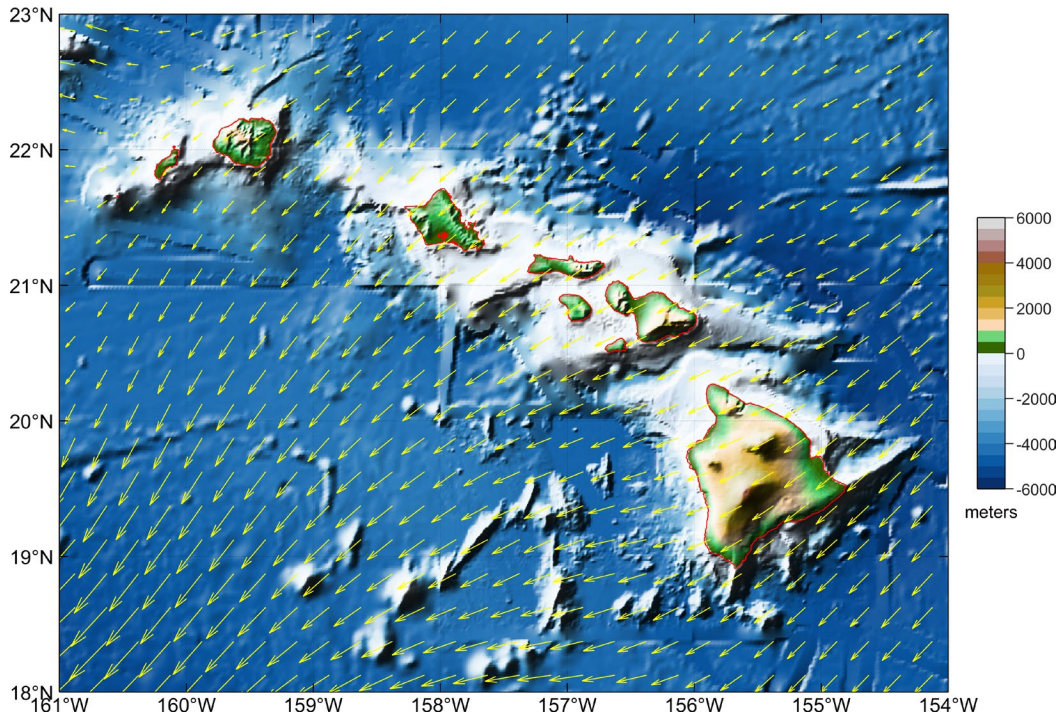
Figure 1. Hawaiian Island topography map and monthly wind field (CCMP Version-3.1 vector wind analyses are produced by Remote Sensing Systems. Data are available at www.remss.com) in March 2023.
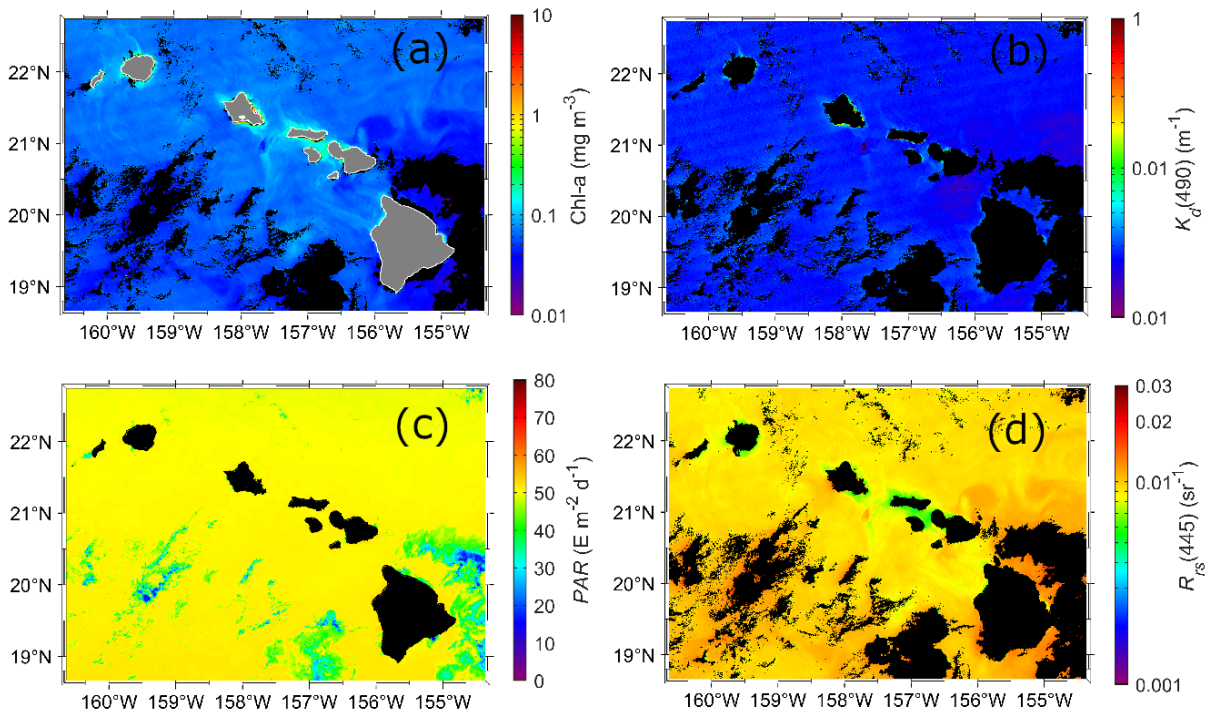
Figure 2. Examples of satellite ocean color data products derived from VIIRS onboard the NOAA-20 satellite for (a) Chl-a, (b) K_d(490), (c) PAR, and (d) R_{rs}(445) (observation time: 23:11–23:13 UTC, March 5, 2022).

3. Cruise participants, measurements, and stations

3.1 Participants

The Hawaii cruise was completed about one year before the federal COVID-19 public health emergency ended. Strict measures were taken before the science crew could board the ship. Seven out of eight individual teams initially planned to participate in the field campaign finally joined with the ship crew to take measurements (Table 1). The City College of New York (CCNY) team was responsible for deploying a hyperspectral polarimetric imaging system. The Lamont-Doherty Earth Observatory (LDEO) team counted, examined, and sized phytoplankton and other detrital particulates. The University of South Florida (USF) team performed above-water and in-water radiometry and water sample analyses for light absorption properties. The NASA Goddard Space Flight Center (GSFC) team took water samples for various biogeochemical measurements and underway above-water radiometry and in-water radiometry. The NOAA Center for Satellite Applications and Research (STAR) team was focused on above-, in-, and on-water radiometry, in addition to general cruise planning and logistic support. The Oregon State University (OSU) team deployed a HyperNAV system along with a conventional radiometric profiler. The University of Miami (UM) team planned to deploy a radiance distribution camera system but gave it up because they were not able to get on the ship due to the COVID-19 measures. The Navel Research Laboratory (NRL) team collected above- and on-water radiometry along with teaming with the NASA team members to setup, maintain, and operate the underway bio-optical flowthrough system. It is noted that the radiometric observations overlapped each other in their functionality and observation time, which can be used to assess the radiometric measurement uncertainties. Fifteen participants from seven individual institutions worked as a team to ensure the success of the field campaign (Table 2). Among them were two PhD students in training and one PostDoc researcher.

Table 1. Principal investigators (PIs) of the NOAA VIIRS ocean color Cal/Val Hawaii cruise (alphabetical order).

Name (Last, First)	Affiliation	Affiliation abbreviation
Gilerson, Alexander	City College of New York	CCNY
Goes, Joaquim	Lamont-Doherty Earth Observatory	LDEO
Hu, Chuanmin	University of South Florida	USF
Ladner, Sherwin	Naval Research Laboratory	NRL
Mannino, Antonio	NASA Goddard Space Flight Center	NASA GSFC
Ondrusek, Michael	NOAA Center for Satellite Applications and Research	NOAA STAR
Tufillaro, Nicholas	Oregon State University	OSU
Voss, Kenneth	University of Miami	UM

Table 2. List of science party personnel aboard the NOAA Ship *Oscar Elton Sette* (grouped by affiliations).

Name (Last, First)	Title	Affiliation
Kovach, Charles	Researcher	NOAA Center for Satellite Applications and Research
Ondrusek, Michael	Chief scientist	NOAA Center for Satellite Applications and Research
Stengel, Eric	Researcher	NOAA Center for Satellite Applications and Research
Ladner, Sherwin	Researcher	Naval Research Laboratory
Bailess, Alex	Researcher	Oregon State University
Belmonte, Adam	Researcher	Oregon State University
Shi, Jing	Student	University of South Florida
Yao, Yao	Student	University of South Florida
Wu, Jinghui	PostDoc	Lamont-Doherty Earth Observatory
Herrera, Eder	Researcher	City College of New York
Malinowski,	Researcher	City College of New York
Freeman, Scott	Researcher	NASA Goddard Space Flight Center
Chaves, Joaquín	Researcher	NASA Goddard Space Flight Center
Farr, Declan	Researcher	NASA Goddard Space Flight Center
Smith, Harrison	Researcher	NASA Goddard Space Flight Center
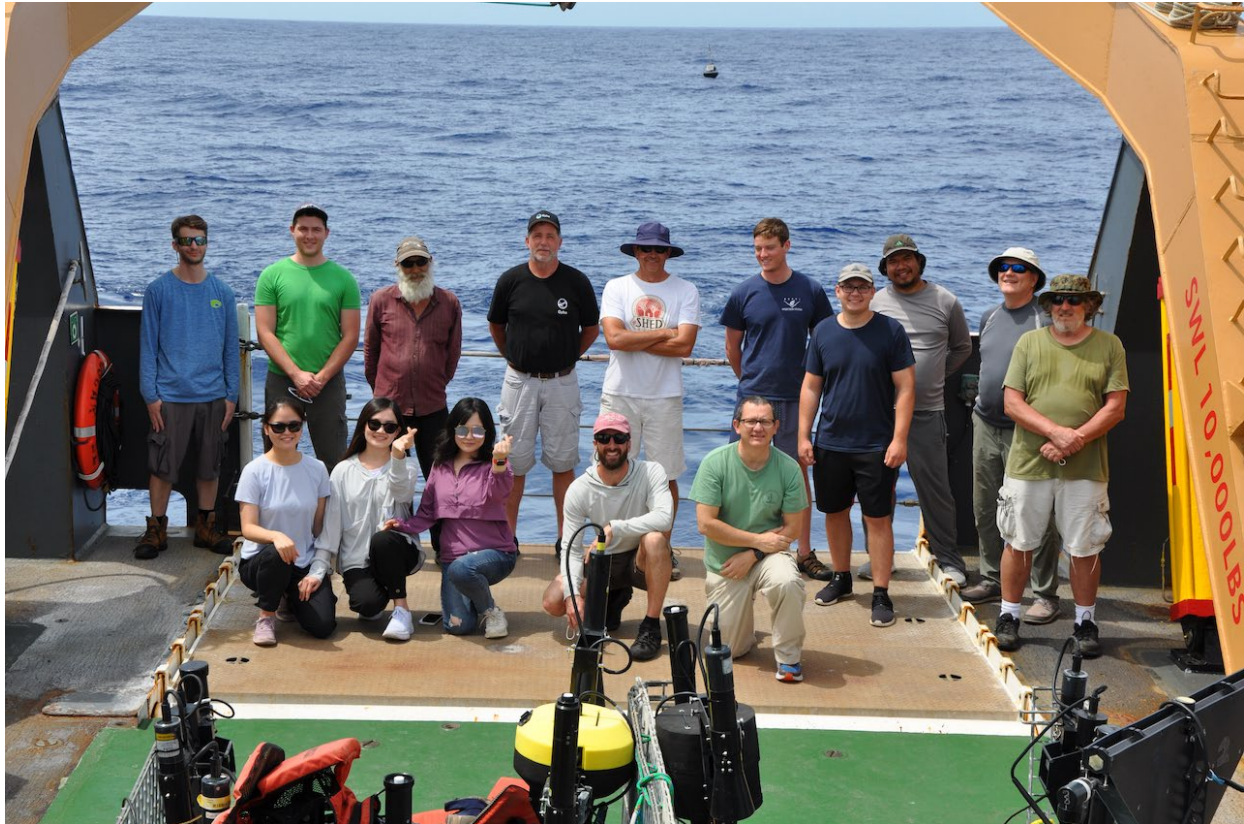
Figure 3. A group photo of the cruise participants with the MOBY system seen in the background ocean (Back row starting from left: Harrison Smith, Declan Farr, Charles Kovach, Sherwin Ladner, Eric Stengel, Alex Bailess, Mateusz Malinowski, Eder Herrera, Scott Freeman, Michael Ondrusek; front row starting from left: Yao Yao, Jing Shi, Jinghui Wu, Adam Belmonte, and Joaquín Chaves). Photo credit: Sherwin Ladner, Naval Research Laboratories.

3.2 Cruise timeline

As a result of COVID-19 protocols, the NOAA STAR team (Michael Ondrusek, Eric Stengel, and Charles Kovach), the NRL team (Sherwin Ladner), and the UM team (Riley Blocker) were forced to miss the first five days of the cruise, while Riley had to miss the whole cruise. The NOAA Ship *Oscar Elton Sette* was originally scheduled to depart on March 7, 2022, but it was delayed one day due to the Covid-19 contact regulations. From March 8 to March 13, Scott Freeman from NASA assumed the role of chief scientist in the absence of Michael Ondrusek, who instead provided daily planning support from shore. With the short-handed science crew, the ship was able to conduct one station at the old MOBY site in the morning and one in the afternoon of the 9th then was required to return to Oahu overnight to pick up a part for the ship. The ship did not get back out to the MOBY site for a new MOBY station until the afternoon of the 10th. On the 11th, the team conducted one morning station at the old MOBY then one afternoon station at the old MOBY. On the 12th, the team conducted two stations at the Hawaii Ocean Time-series (HOT) site north of Oahu. On the 13th, the ship returned to Oahu to pick up the NOAA and NRL Teams to join the remainder of the cruise. Again, due to the COVID-19 protocols, Riley Blocker was forced to miss

the rest of the cruise. Due to the amount of time it took to pick up the rest of the crew, only one station could be sampled off the coast of Oahu on the afternoon of the 13th. On the 14th, one station was sampled in the morning at the new MOBY site, and then three stations were conducted the rest of the day at the old MOBY site. On the 15th, one station was conducted at the old MOBY site, and then three stations at the new MOBY site. On the 16th, efforts were concentrated on characterizing the new MOBY by conducting continuous measurements grouped into three stations at the new site. On the 17th, one station was conducted at the old MOBY site, and then two stations at the new MOBY site. As the ship had to return early on the 18th into port, only one station could be sampled in the morning just south of Oahu. Table 3 briefly describes the major activities of the Hawaii cruise.

Table 3. Timeline and major activities of the Hawaii cruise

Day	Main activities
3/7/2022	Onboard; ship decided not to go out
3/8/2022	Ship left port and steamed to MOBY
3/9/2022	MOBY-old site in the morning and after; ship drills in between; then steamed to Oahu to pick up ship part overnight.
3/10/2022	MOBY-refresh site in the afternoon
3/11/2022	MOBY-refresh site in the morning, MOBY-old site in the afternoon
3/12/2022	Conducted two stations at the HOT site
3/13/2022	Picked up science crews and conducted an afternoon station off the coast of Oahu
3/14/2022	MOBY-refresh site in the morning and three measurements at MOBY-old site
3/15/2022	MOBY-old site in the morning and then three MOBY-refresh site in the afternoon
3/16/2022	Three stations at MOBY-refresh site
3/17/2022	One station at MOBY-old site and then two stations at MOBY-refresh site
3/18/2022	One last station off Oahu

3.3 Sampling stations

The stations were distributed over a triangular region around Oahu, stretching from the north at the HOT station, to the south of Oahu, and to Lanai, where two MOBY systems were moored concurrently (Figure 4). Most of the stations occurred around MOBY stations. At every station, a CTD rosette system was deployed to obtain water samples that were treated and stored for later analyses, including Chl-a, SPM, particulate organic carbon (POC), colored dissolved organic

carbon (CDOM), light absorption coefficient for phytoplankton ($a_{ph}(\lambda)$), high-performance liquid chromatography (HPLC), particle counting, sizing, and imaging, etc. The water radiometric properties were measured using multiple instruments almost simultaneously. A summary of water sampling stations is given in Table 4.

Table 4. Observation stations and environmental conditions

Station	Date	Time (local)	Latitude	Longitude	Wind (kn)	Seas (ft)	Clouds (%)	Solar Zenith	Location
1	3/9/2022	1300	20.822	-157.191	5	3	20	25.6	Old Moby
2	3/9/2022	1535	20.808	-157.181	11	1	20	49.8	Old Moby
3	3/10/2022	1500	20.706	-157.144	8	1	20	42.4	New Moby
4	3/11/2022	1039	20.720	-157.143	3	2	10	38.0	New Moby
5	3/11/2022	1326	20.820	-157.181	11	1	40	26.9	Old Moby
6	3/12/2022	1048	22.756	-157.933	15	4	10	37.8	Sta. Aloha
7	3/12/2022	1445	22.474	-157.641	15	4	60	39.7	N. of Oahu
8	3/13/2022	1240	21.218	-158.459	13	2	10	23.9	SW Oahu
9	3/13/2022	1600	21.213	-158.620	2	3	20	53.6	SW Oahu
10	3/14/2022	1055	20.733	-157.136	3	3	40	34.1	New Moby
11	3/14/2022	1255	20.828	-157.179	3	3	30	23.5	Old Moby
12	3/14/2022	1541	20.837	-157.188	6	2	40	50.4	Old Moby
13	3/14/2022	1826	20.861	-157.208	10	2	30	86.4	Old Moby
14	3/15/2022	1040	20.841	-157.208	1	2	60	36.7	Old Moby
15	3/15/2022	1229	20.730	-157.138	6	2	60	22.7	New Moby
16	3/15/2022	1356	20.724	-157.133	5	2	60	29.7	New Moby
17	3/15/2022	1646	20.719	-157.132	13	5	50	64.8	New Moby
18	3/16/2022	1155	20.729	-157.148	17	5	50	24.5	New Moby
19	3/16/2022	1316	20.732	-157.142	10	3	40	24.2	New Moby
20	3/16/2022	1649	20.740	-157.137	4	2	80	65.4	New Moby
21	3/17/2022	1030	20.836	-157.204	6	2	80	38.0	Old Moby
22	3/17/2022	1201	20.731	-157.154	9	5	80	23.5	New Moby
23	3/17/2022	1524	20.738	-157.139	6	2	80	46.3	New Moby
24	3/18/2022	1054	21.111	-158.062	4	2	10	33.9	S. of Oahu
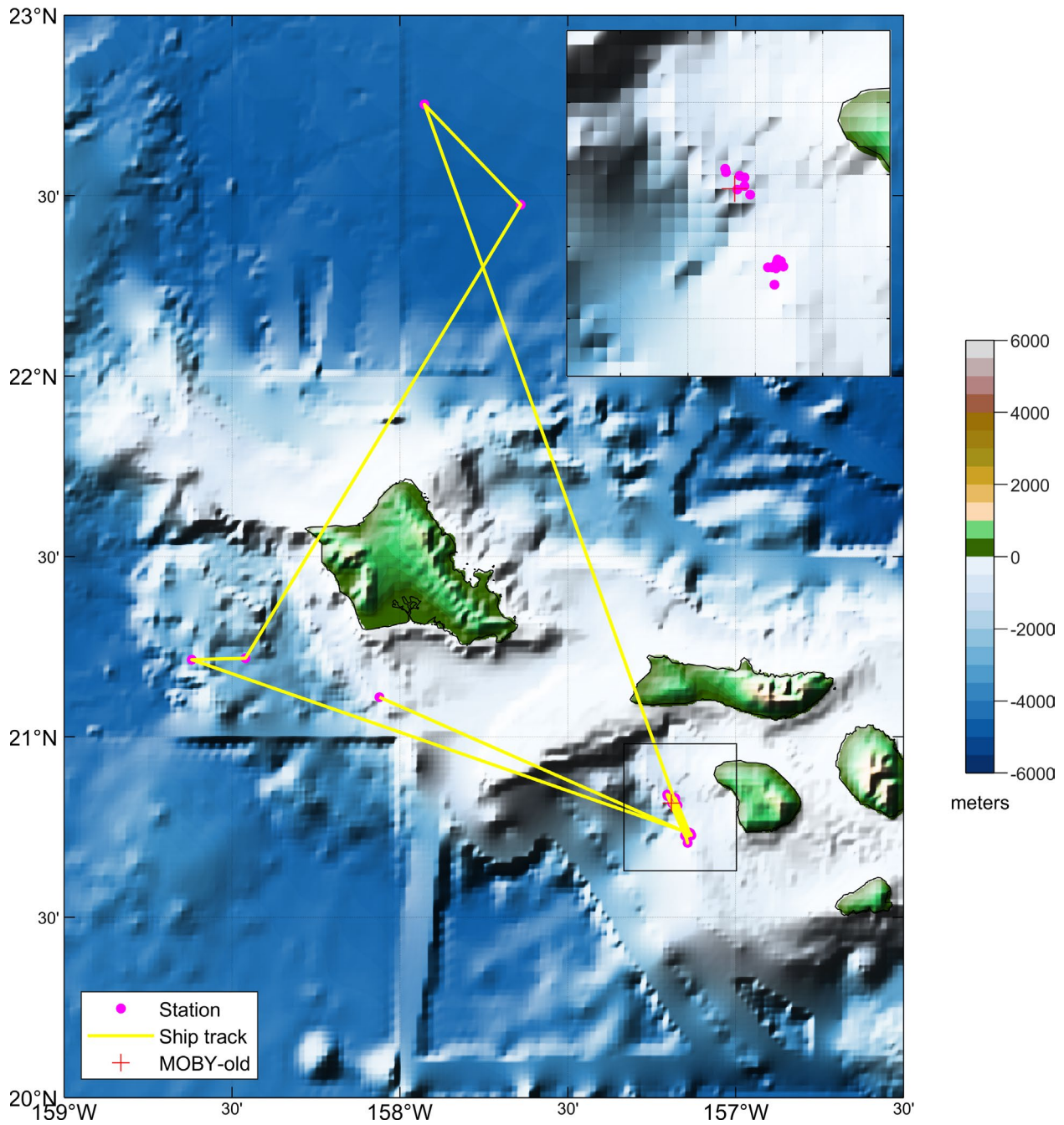
Figure 4. The VIIRS ocean color Cal/Val cruise tracks and stations in the Hawaiian Islands in March 2022. The insert depicts the sampling stations clustered around the MOBY stations: the old MOBY site is in the north, and the refresh MOBY site is located to the south (not marked in the map but approximately located near the cluster of stations in the south).

4. Field activities by individual teams

4.1 STAR team – Michael Ondrusek, Eric Stengel, and Charles Kovach

The NOAA/STAR team operated three radiometers for water optical radiometry measurements and one instrument for aerosol observations. In addition, the team coordinated the cruise logistics and daily science operations.

4.1.1 Radiometric calibration

The NOAA/STAR team conducted pre- and post-cruise calibrations of the in-water radiometers, except for the HyperNAV and C-OPS sensors in College Park, MD. Radiance sensors were calibrated with a NIST traceable Optronic Laboratories OL-455 integrating sphere. Irradiance sensors were calibrated with a NIST traceable FEL type 1000 W standard irradiance lamp. On February 15, 2022, seven Satlantic/Seabird OCR radiometers and thirteen Satlantic/Seabird OCI irradiance sensors were calibrated. Post-cruise, on April 14, 2022, eight radiance and 14 irradiance sensors were calibrated.

4.1.2 In-water radiometric profiler

One in-water Satlantic/Seabird HyperPro-II radiometer system was deployed in a profiling mode (Figure 5). The profiler system (s/n 179) was equipped with a downward-looking OCR radiance sensor (s/n 206) and an upward-pointing OCI irradiance sensor (s/n 233). Downwelling surface irradiance was measured with an E_s sensor (s/n 234) mounted atop the grappa pole on deck (Figure 7). The system also had one ECO-Puck sensor (SATB2F1492) that measured fluorescence to estimate Chl-a and $b_{bp}(\lambda)$ at 470 nm and 532 nm. It also measured ancillary parameters, including water depth, temperature, and instrument tilt. The profiler was deployed simultaneously at all stations from March 14th on with the USF and OSU HyperPro-II instruments and the NASA C-OPS (Figure 5), following the multicast deployment method. During deployment, the raw data were continuously logged while each instrument was profiled 3 to 5 times down to 15 meters. This process was further replicated for 3 to 5 casts at each station.

Figure 5. The simultaneous deployment of HyperPro-II profilers and C-OPS.

4.1.3 Skylight-blocking radiometry measurements

The NOAA team had two HyperPro-II systems deployed as skylight-blocking apparatus (SBA) (Figure 6). One system consisted of the NOAA profiler (s/n 086) outfitted with one radiance sensor (s/n 416), one irradiance sensor (s/n 530), and NASA's SBA cone adaptors. The above-water irradiance was measured aboard the ship with the NOAA irradiance sensor (s/n 531). The second SBA system deployed by NOAA was from the University of Massachusetts Boston (UMB). The SBA floaters were deployed at every station after the NOAA/STAR team joined the cruise on March 14, 2022.

Figure 6. Simultaneous deployment of two SBAs (left and middle) and one HyperNAV (right).
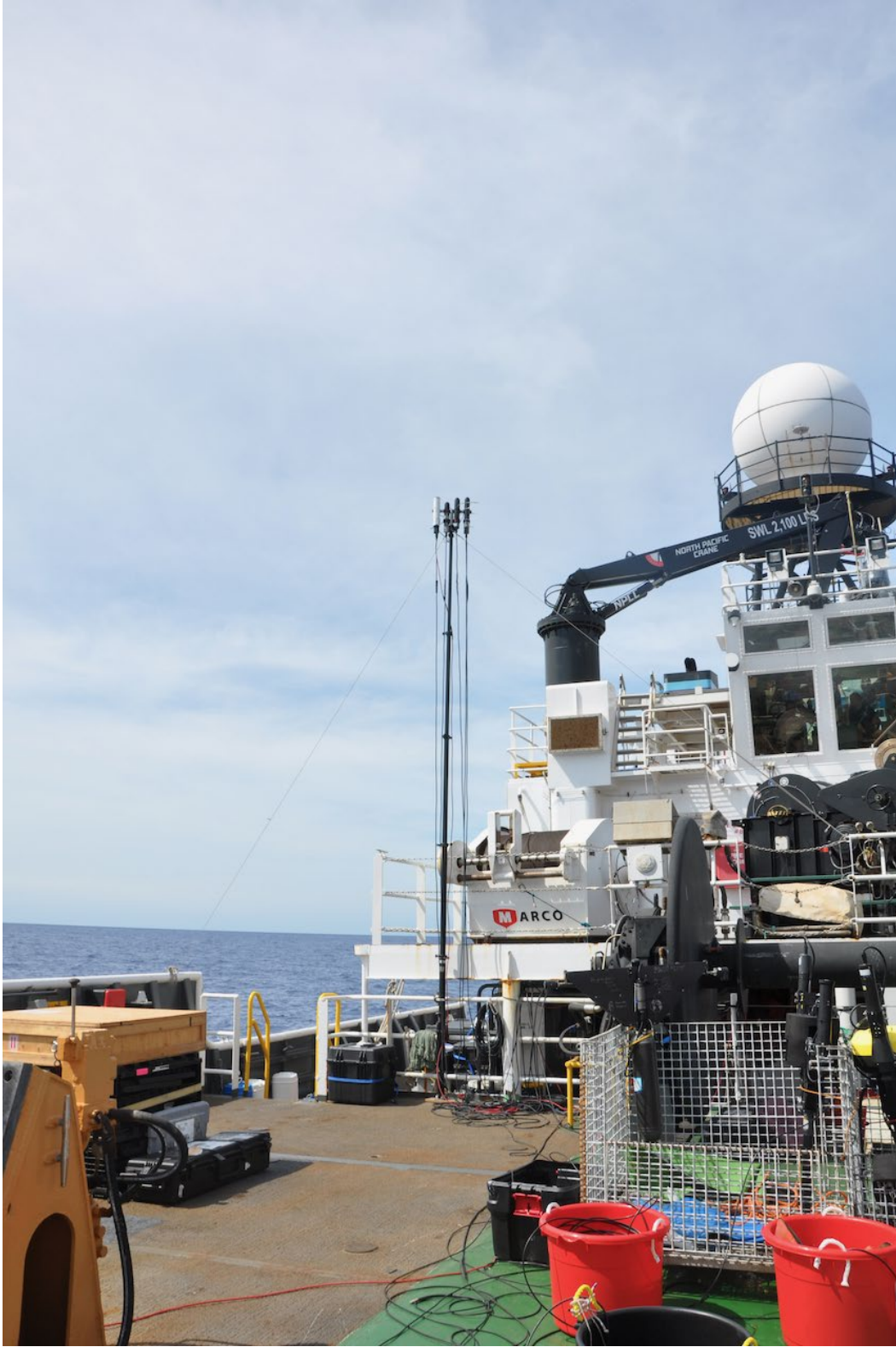
Figure 7. Above-water irradiance sensors mounted atop the telescoping pole.

4.1.4 Above-water radiometers for water-leaving radiance

NOAA/STAR team deployed two above-water handheld instruments after joining the cruise on March 13th. One system was the ASD HandHeld2 and the other was the Spectra Vista 512i. The ASD has a spectral range of 325 nm to 1075 nm and a spectral resolution of less than 3 nm. This unit was equipped with a built-in GPS and fore-optics with a 10° field of view (FOV). The other system was a Spectra Vista HR-512i. The HR-512i covers a spectral range of 350 nm to 1050 nm, with a 3 nm spectral resolution and an 8° FOV. ASD measurements were only conducted at the first two stations, while HR-512i measurements were run at all stations. Validation measurements were conducted on the bow simultaneously with the other team members' above-water measurements, while the floaters and profilers were typically already in the waters. The method of Mueller et al. (2003b) was utilized with a NOAA Spectralon white plaque that has a nominal reflectance of 0.99. The water and plaque measurements were conducted at 40°–45° from the nadir and an azimuth angle of 90° to 135° to the sun. The sky was measured at a 40° to 45° zenith angle and azimuth angle of 90° to 135° to the sun.

4.1.5 Aerosol optical thickness

AOT was measured at 11 stations using a Microtops sunphotometer. The data were delivered to NASA for processing as part of the AERONET Marine Aerosol Network program (https://aeronet.gsfc.nasa.gov/new_web/cruises_v3/Oscar_Elton_Sette_22.html).

4.2 NRL team – Sherwin Ladner

The NRL team arrived in Hawaii on March 4, 2022. COVID tests were administered prior to departure on March 7, 2022. NRL was considered to be in close contact with positive personnel and was quarantined onshore for seven days. A second COVID test was administered on March 13, 2022, and NRL was allowed to board the ship. NRL collected above-water $R_{rs}(\lambda)$ measurements aboard the NOAA Ship *Oscar Elton Sette* at 16 station locations from March 13–18, 2022, represented by white circles in Figure 8. Four stations (11, 12, 13, and 20) were collected in the vicinity of the original MOBY mooring (MO), nine stations (10, 14, 15, 17, 18, 19, 21, 22, 23) near the MOBY refresh mooring (MN) and three stations (8, 9, 24) near Oahu. Stations were adaptively planned and selected based on predicted (https://www.windy.com) weather forecasts and clear sky conditions to increase the probability of obtaining satellite matchups. NRL, with assistance from NASA (Scott Freeman and Harrison Smith), also collected continuous underway hyperspectral IOPs using the ship's seawater flow-through system. In addition, NRL provided individual daily Google Earth chlorophyll-a images for VIIRS sensors (SNPP and NOAA-20) in near real-time along with daily composites that consisted of merging VIIRS/SNPP, VIIRS/NOAA-20, OLCI/Sentinel-3A, and OLCI/Sentinel-3B to plan next day's station locations and to determine if daily stations collected yielded valid sensor matchups.
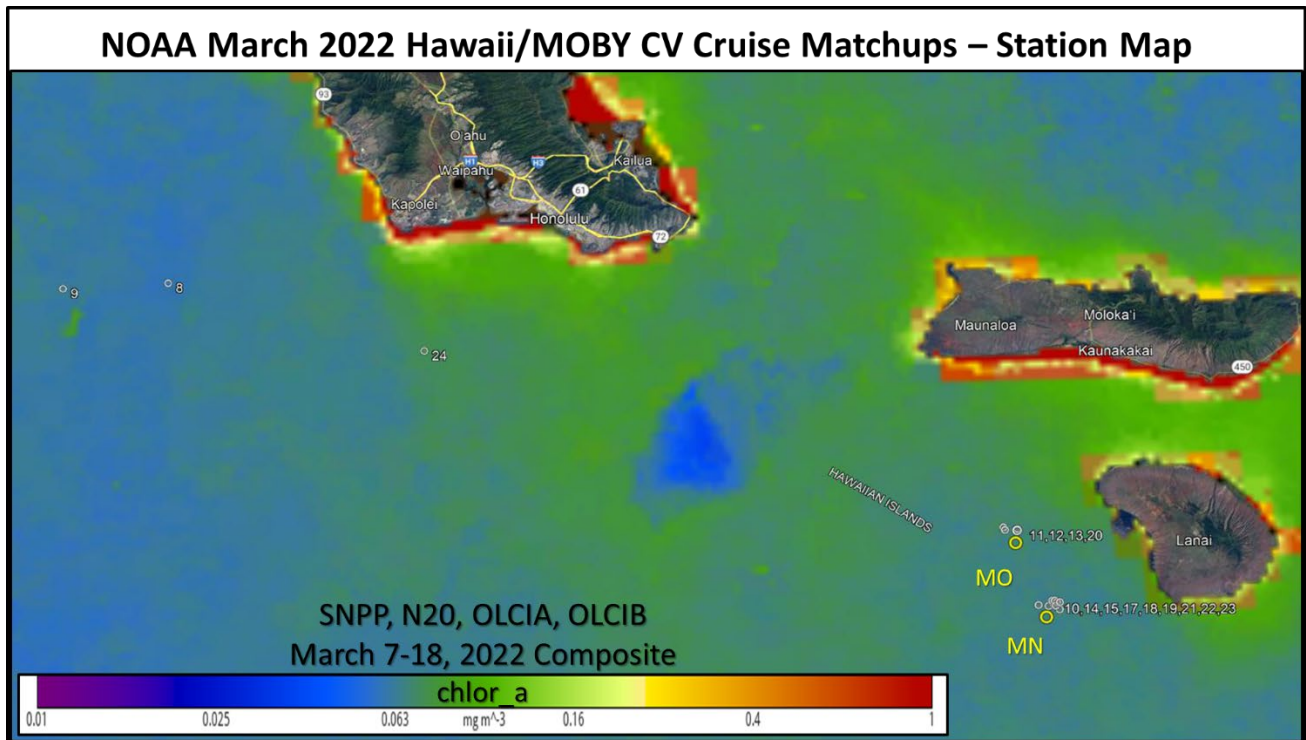
Figure 8. Multi-sensor (SNPP, NOAA-20, OLCIA, and OLCIB) merged Chl-a composite from March 7 through March 18, illustrating the 16 station locations (Stations 8–15, 17–24) collected by NRL aboard the NOAA Ship *Oscar Elton Sette*. NRL's Automated Processing System (APS) processed the composite image, and all sensors were vicariously calibrated using MOBY data annually.

NRL measurements included: 1) above-water hyperspectral $R_{rs}(\lambda)$ using two handheld hyperspectral radiometers and 2) continuous underway hyperspectral IOPs from the ship's seawater flow-through system.

4.2.1 Above-water radiometry measurements

Above-water remote sensing reflectance measurements were taken using Analytical Spectral Devices FieldSpec Handheld-2 hyperspectral spectroradiometer (ASD) and Spectral Evolution PSR-1100F hyperspectral spectroradiometer (SEI). Each spectroradiometer was calibrated for spectral radiance using NIST-traceable standards by the respective manufacturers. The bow location was selected for collection to reduce the contamination from the ship's structure on the collection of the calibrated reference plaques (NRL's 10-inch white Labsphere calibration/reference plaque with NIST certification) and the water's surface.

Above water measurements were acquired at 16 stations using the ASD and SEI spectroradiometers. All above water measurements were made using the NRL white 99% reflectivity 10-inch plaque during the standard sky, water, and reference plaque sequence for deriving the above-water $R_{rs}(\lambda)$. The white plaque has a known BRDF surface and is used to normalize the un-calibrated irradiance measurements for E_s. Answers may vary due to instrument type and calibration, warm-up time, shadowing of the plaques, variable light field, etc.

The above-water measurement activities took place on the bow of the NOAA Ship *Oscar Elton Sette*. At the start of each station, the reference plaque was placed on the bow's bollard posts (Figure 9). The plaque was occasionally partially obscured from the full hemisphere by the ship's bridge, participants, cloud cover, and the bow rail. The magnitude of this bias will depend on how much of the diffuse component is blocked. Optimal and non-variable light conditions were sought for the sky, water, and reference measurements for the complete sequence. NRL recorded station metadata (time, latitude, longitude, instrument base filenames, spectra target assignments and numbers, ocean parameters from ship's flow-through, physical water characteristics, and meteorology) on hand written log sheets during each station and later compiled into an Excel spreadsheet by Charles Kovach (NOAA). Other personnel took photographs of the sky and water surface conditions and the participants in action. All groups in attendance attempted to make concurrent measurements using multiple above-water spectroradiometers (ASD, Spectral Evolution, GER, and SVC). At the end of each station, the plaque and instruments were powered off and placed in a water-tight storage box on the bow. At the end of each day, they were taken back into the lab to download data and stored in their respective cases.
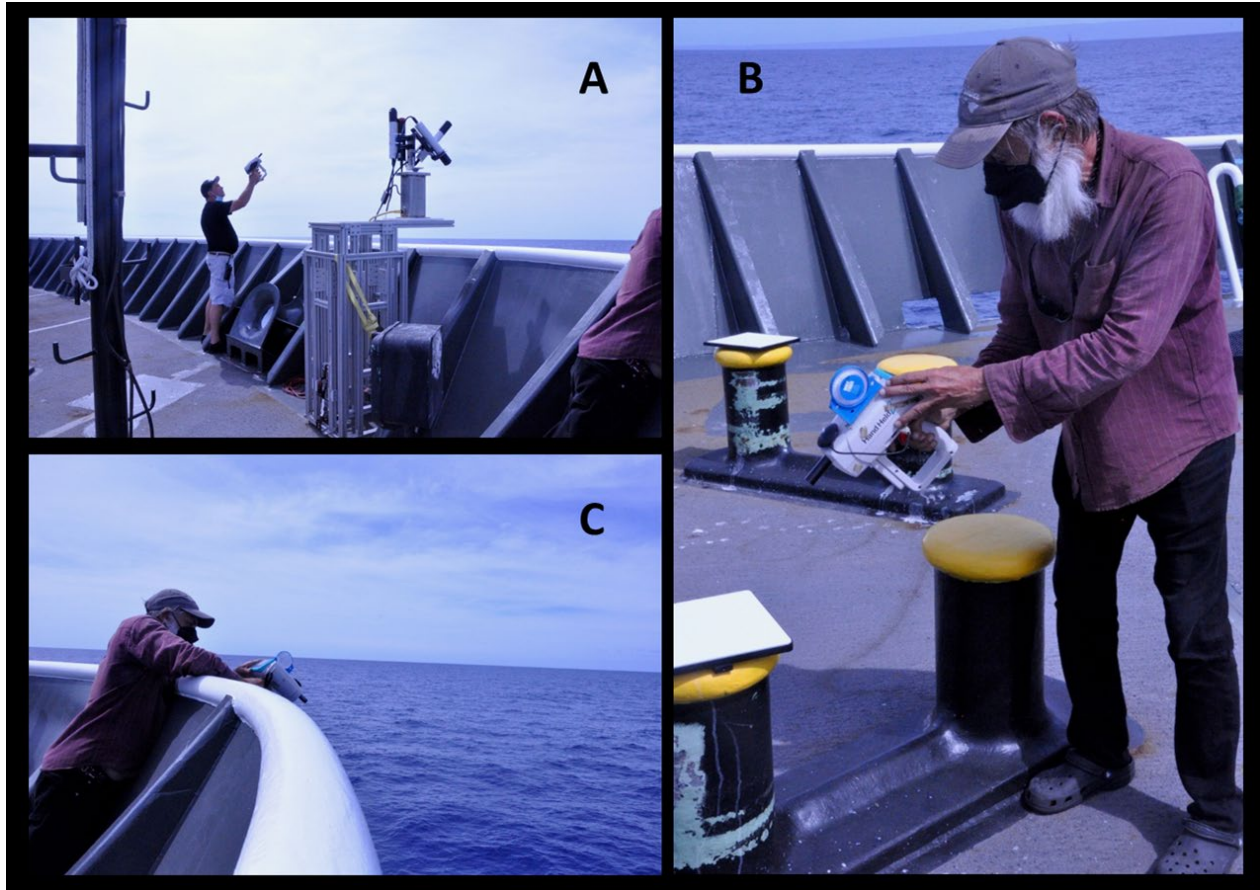
Figure 9. Illustration of the station collection sequence for above-water R_{rs}. (A) Sherwin Ladner (NRL) was collecting the sky measurement sequence. (B) Charles Kovach (NOAA) was collecting the white reference plaque sequence, and (C) Charles Kovach (NOAA) was collecting the water sequence. The above-water spectroradiometer shown in all images is the ASD with an inclinometer attached to maintain the desired measurement angle of 40°.

The NRL group ASD instrument was configured to average five spectra per scan and save five spectra scans for each of the three targets (sky, reference, and water). The SEI is designed to collect one spectrum at a time and has to be triggered for each individual scan (10 scans per target). During each station, five consecutive radiometric spectra with subtracted dark measurements were taken of each of the following targets: 1) sky, 2) NRL white plaque, and 3) water for the ASD. The same sequence was collected for the SEI with 10 radiometric spectra per target. For both the ASD and SEI instruments, an 8° fore optic was attached, and the integration time was optimized for each target prior to collection (i.e., the integration time of the sensor was changed based on the relative brightness of the target and new dark counts were taken to correct for instrument noise). The sensor zenith angles for the θ_p, θ_{sfc}, and θ_{sky} measurements were 40°, 40° and 40°, respectively. The relative azimuth angle of the sensor to the sun ranged from 90° to 135° depending on visual surface contamination (sea foam, glint, bubble, shadows, etc.). The post-processing of the ASD and SEI above-water data collected by NRL was performed using code developed by NRL for the 16 stations collected, and $R_{rs}(\lambda)$ was computed using the NRL white plaque using the same collection

protocols for both instruments to look at inter-sensor differences. The NRL software was modified to process the above water instruments using a NIR baseline-subtraction protocol and the calculation of the surface reflectance correction ρ, based on the solar azimuth and wind speed calculation (Mobley, 2015). This approach is a substantial improvement over using a constant ρ of 0.021 to minimize the reflected sunlight contribution.

4.2.2 Above-water processing protocols

The ASD spectroradiometer measures light at 1.0 nm sampling over the 325 nm to 1075 nm spectral range. The SEI spectroradiometer measures light at 1.0 nm sampling over the 320 nm to 1100 nm spectral range. Processing follows the equation:

$$R_{rs} = \frac{L_{w+s} - L_{sky}\rho(\theta)}{\pi L_p \, / \, refl} \tag{1}$$

where:

- L_{w+s} is the measured signal from the water and includes both L_w and reflected skylight;
- L_{sky} is the measured signal from the sky;
- L_p is the average measured signal from the white Spectralon plaque;
- $refl$ is the reflectivity of the plaque (approximately 99% white; actual measured spectral values are used in the calculation);
- πL_p converts the reflected radiance values to irradiance for these "Lambertian" diffusers;
- The measured sky radiance is multiplied by $\rho(\theta)$, which is the proportionality factor that relates the radiance measured when the detector views the sky to the reflected sky radiance measured when the detector views the sea surface.

The value of $\rho(\theta)$ is dependent on wind speed and direction, detector FOV, and sky radiance distribution. Only in the case of a level sea surface and a uniform sky radiance distribution does $\rho(\theta)$ equal the average of the Fresnel reflectance over the detector FOV. For our measurement angles under nominal sky and wind conditions, we pull $\rho(\theta)$ from the table of Mobley (2015).

The computed $R_{rs}(\lambda)$ is assumed to be "black" at about 750 nm due to water absorption. If not zero, then it is assumed that the L_{sky} was not estimated correctly. Following the "quick and easy" algorithm (Carder and Steward, 1985), it further assumes that any error in the skylight reflection term is white (not wavelength dependent), and one may simply subtract the computed $R_{rs}(750)$ from the entire spectrum. In practice, this may lead to negative reflectance values near 750 nm. Therefore, the processing subtracts the smallest $R_{rs}(\lambda)$ in the range of 700–800 nm (Figure 10).
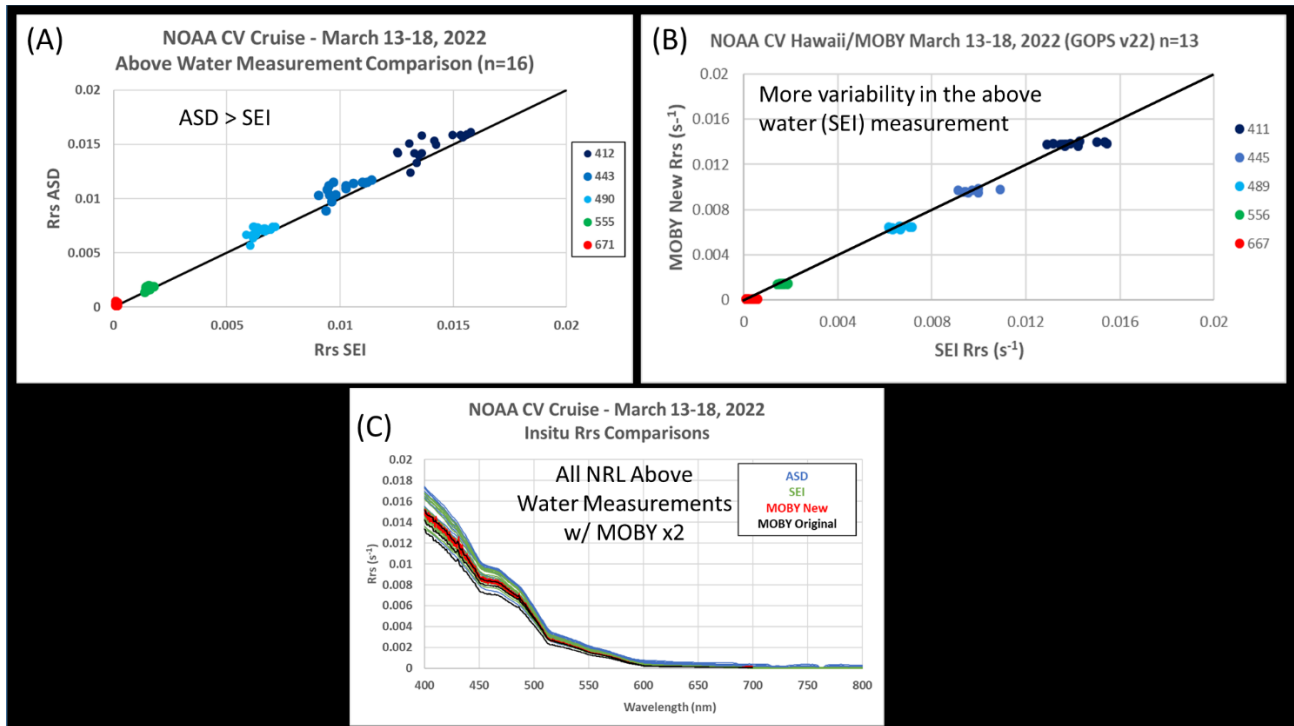
Figure 10. (A) Preliminary spectral $R_{rs}(\lambda)$ comparisons between above-water handheld ASD and Spectral Evolution (SEI) spectroradiometers at VIIRS wavelengths for all 16 stations. The ASD measurements are slightly higher than the SEI. (B) Preliminary spectral $R_{rs}(\lambda)$ comparisons for the SEI and the MOBY refresh mooring. The SEI $R_{rs}(\lambda)$ show more variability than the MOBY $R_{rs}(\lambda)$. (C) Preliminary hyperspectral $R_{rs}(\lambda)$ plot of the ASD (blue), SEI (green), MOBY refresh mooring (red), and the MOBY original mooring (black) for all stations collected near the MOBY moorings. The MOBY refresh mooring data (red) show the least $R_{rs}(\lambda)$ variability, while the above water measurements show the most variability.

4.2.3 Continuous underway flow-through measurements of IOPs

IOP flow-through measurements were collected to address specific objectives as follows but will be used for other analyses as well:

- Characterize the spatial variability of IOPs (a_t, a_p, b converted to b_b, c) along the cruise track and how the variability impacts the uncertainty of in situ measurements at each station along with sub-pixel variability.
- Evaluate the vertical optical changes within one optical depth (penetration depth of satellite observations) in coastal and offshore waters. The flow-through data at a source depth of 3 m can be different from observed satellite values. Vertical IOP profiles can be used to evaluate the vertical changes and the effect on surface IOP validation.
- Determine the a and c properties at specific wavelengths to validate the IOPs derived from the VIIRS ocean color satellites.

- Determine the optical water mass characteristics using spectral scattering and absorption to identify the response of ocean color.
- Define coastal/shelf frontal boundaries, ocean processes, and water mass types.

IOPs were collected continuously using an underway flow-through system designed, set up, and operated by NASA (Scott Freeman and Harrison Smith) and NRL (Sherwin Ladner), including one unfiltered Sea-Bird hyperspectral ac-s instrument for total absorption and beam attenuation, Sea-Bird BB3 instrument for backscattering designed with three channels (440 nm, 532 nm, and 650 nm) and the ship's GPS and Thermo-Salinograph (CTD) connected to the ship's seawater flow-through system where the water intake was located at approximately 3 m below ocean surface. We had to wait initially for the ship to add another water source for the BB3 instrument due to reduced water flow for the ac-s and other groups' instruments. Initially, all instruments were running off the same water source. The BB3 instrument was inserted and started logging on March 15, 2022. To ensure stability and reliability, we placed the ac-s in a controlled water bath to dissipate the instruments' heat and stabilize their temperature (Figure 11). A total of two ac-s instruments (s/n 316, s/n 300 - backup) were available from NRL for use during the cruise.
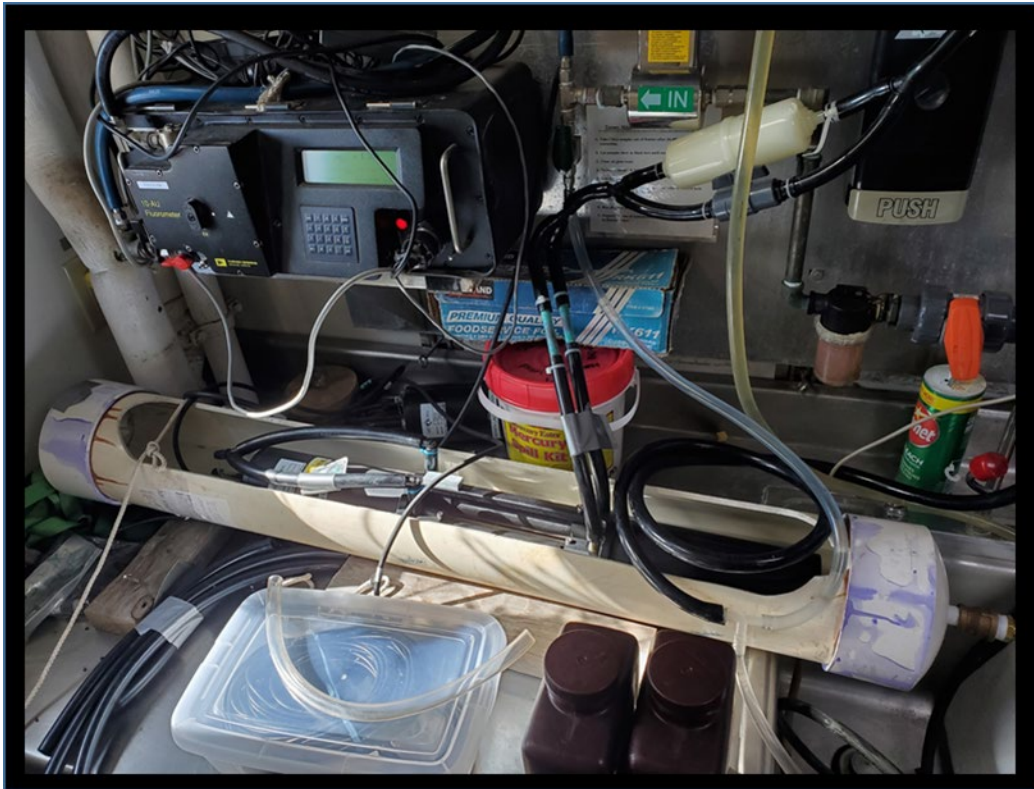
Figure 11. The NRL IOP continuous flow-through wet lab setup on the NOAA Ship *Oscar Elton Sette* included a hyperspectral ac-s instrument (non-filtered) and a BB3 sensor. The ac-s instrument was placed inside a PVC tube water bath to maintain a constant temperature during operation and was calibrated with Nanopure water before and after the cruise. The BB3 instrument was placed inside a flow cell. The PVC tubes and the BB3 flow cells were designed specifically for those instruments.

The ac-s and BB3 were interfaced with a Sea-Bird DH4 data logger with additional inputs from the ship's flow-through system (CTD and GPS). The ship's flow-through system data streams included position, time, date, heading, water temperature, and salinity. These CTD inputs are required for the standard processing protocol corrections during the post-processing of the ac-s data. The WET Labs DH4 host software (WLHOST) combines and stores all these data inputs and allows a WetView display capability in real-time to evaluate the ac-s data to ensure the instruments are operating correctly and producing reliable and consistent data. The data sample rate of the ac-s meters was 4 Hz. Output data files from the DH4 were saved hourly for the entire cruise.

The ac-s sensor was cleaned and calibrated by Scott Freeman (NASA) at the end of the cruise. Calibration of the ac-s instrument included running Nanopure water through the instruments using a gravity feed. This clean water calibration was done after cleaning the absorption and scattering tubes. The BB3 instrument was also calibrated at the end of the cruise by placing black electrical tape over the sensors for 5 minutes to get a dark reading for post-processing corrections.
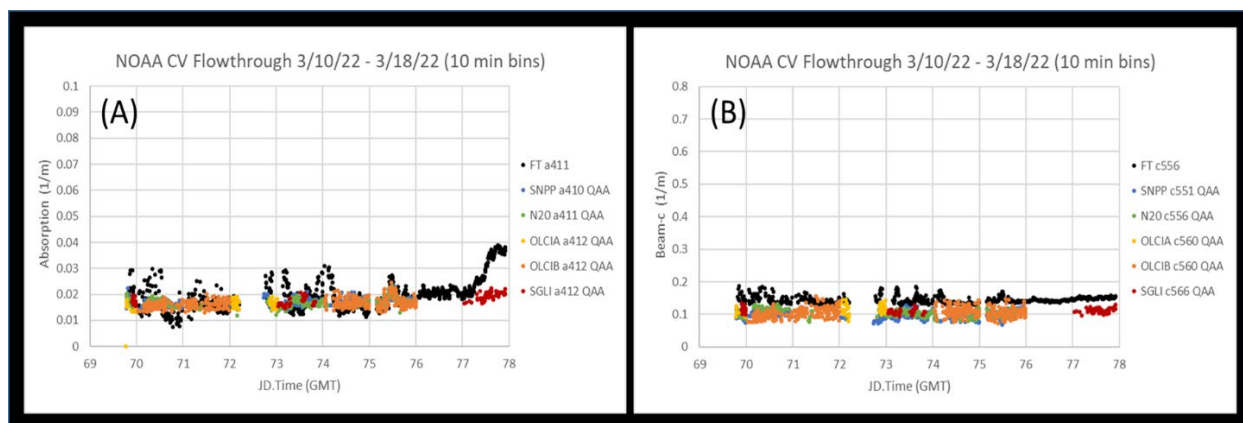
Figure 12. (A) Preliminary comparison between NRL APS processed VIIRS/SNPP (blue) and VIIRS/NOAA-20 (green), OLCI/Sentinel-3A ("OLCIA" in yellow) and OLCI/Sentinel-3B ("OLCIB" in orange), and SGLI/GCOM-C (red) and flow-through total absorption at 410 nm for entire cruise track (JulianDay.Time = x-axis). (B) Same as (A) but for beam attenuation at 551 nm. Total absorption at 410 nm between the flow-through and satellites agrees very well, while the beam attenuation at 551 is slightly underestimated by the satellites. All satellites are vicariously calibrated at the MOBY mooring and show good agreement for both IOP properties.

The hyperspectral ac-s instrument measures $c(\lambda)$ and $a(\lambda)$ from 399 nm to 755 nm at 4.0 nm spacing, and the BB3 instrument returns total volume scattering (β), volume scattering of particles (β_p), backscattering of particles (b_{bp}) and b_b at three channels (440 nm, 532 nm, and 650 nm). Concurrent flow-through measurements of time, latitude, longitude, temperature, and salinity from a thermos-salinograph (CTD) will be used for correction of the ac-s $a(\lambda)$. Correctly addressing the thermal, salinity, and scattering ($c-a$) corrections that must be applied is important (Röttgers et al., 2013). All the flow-through instruments collected through the DH-4 were time merged using the WET Labs Archive Processing program (WAP), and hourly output archive files were generated (Figure 12). Hourly WAP archive files were then combined to create daily files. The daily WAP

archive files were binned into 1-minute time bins to reduce the amount of data for spreadsheet import and analysis (Figure 13). The standard order of post-processing protocol used:

- Apply temperature and salinity corrections to ac-s a_t data using the coincident ship thermo-salinograph temperature and salinity data.
- Temperature correct pure water calibration data for a_t and c_t.
- Subtract the pure water calibration data from the in situ data.
- Remove spikes in data due to bubbles, etc., using a σ filter and then interpolate.
- Scattering correction following Röttgers et al. (2013).
- Add spectral pure water absorption coefficients (Pope and Fry, 1997) to measured a_{t-w} to yield a_t.
- Compute spectral scattering $b = c_t - a_t$.
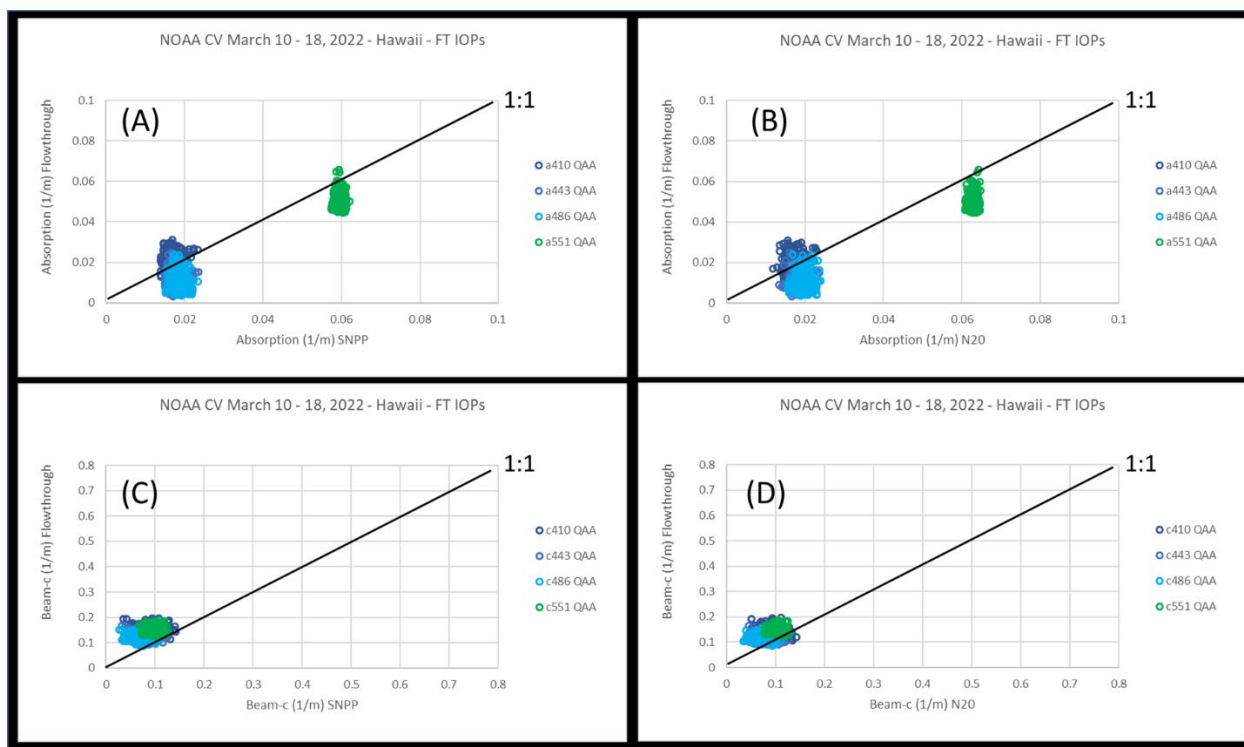
Figure 13. (A) Preliminary total absorption matchups between QAA VIIRS SNPP at 410 (dark blue), 443 (middle blue), 486 (light blue), and 551 nm (green) processed by NRL APS and the IOP flow-through system ac-s. (B) Preliminary total absorption matchups between QAA VIIRS NOAA-20 at 410 (dark blue), 443 (middle blue), 486 (light blue), and 551 nm (green) processed by NRL APS and IOP flow-through system ac-s. (C) Preliminary beam attenuation matchups between QAA VIIRS SNPP at 410 (dark blue), 443 (middle blue), 486 (light blue), and 551 nm (green) processed by NRL APS and IOP flow-through system ac-s. (D) Preliminary beam attenuation matchups between QAA VIIRS NOAA-20 at 410 (dark blue), 443 (middle blue), 486 (light blue), and 551nm (green) processed by NRL APS and IOP flow-through system ac-s. Data from both

satellites and flow-through IOPs are in good agreement. NOAA-20 provides slightly better beam attenuation matchups.

4.3 CCNY team – Alex Gilerson, Eder Herrera, and Mateusz Malinowski

The main instrument of the CCNY team used for above-water observations in the validation process was GER (Spectra Vista, NY). Measurements were also made with the hyperspectral polarimetric imaging system, which included a snapshot hyperspectral imager ULTRIS X20 (Cubert, Germany) and a polarization camera M2450 (Teledyne, DALSA). In addition, AOT was measured with a Microtops II sunphotometer (Solar Light, PA) at five wavelengths of 380, 500, 675, 870, and 1020 nm.

4.3.1 Handheld spectroradiometer

The GER 1500, Field Portable Spectroradiometer, is a hand-held spectroradiometer designed to provide fast spectral measurements covering the UV, visible, and NIR wavelengths from 350 to 1050 nm at 3 nm (full width at half maximum, FWHM) resolution. It uses a diffraction grating with a silicon diode array with 512 discrete detectors and can read 512 spectral bands. Subsequent downloads and analyses are fulfilled using a personal computer with a standard RS232 serial port and the GER 1500 licensed operating software. The GER 1500 is equipped with a standard lens with a 4° nominal field of view (FOV) for above-water observations. The GER 1500 is used in the field to calculate $R_{rs}(\lambda)$ by measuring the total radiance $L_{surf}(\lambda)$ above the sea surface, the sky radiance ($L_{sky}(\lambda)$), and the downwelling radiance ($L_d(\lambda)$) over a plaque.

The instrument has undergone radiometric and wavelength calibration in the optics mode (with the lens) at the manufacturer in March 2019 and additional tests at CCNY. Generally, due to the nature of the measurement, calibration is not necessary. The main details of the data processing are available in cruise report #4 (Ondrusek et al., 2019), which follows the Mobley (1999) approach.

4.3.2 Hyperspectral polarimetric imaging system

The system (Figure 14) included a snapshot hyperspectral imager with a manually rotatable polarizer and a polarization camera with a filter wheel, which contained color filters. The system was operated by two laptop computers.

- Hyperspectral imager

The imager has a unique capability of simultaneously recording data from 410×410 pixels, FOV = 35° in the hyperspectral mode for each pixel with 164 bands in the 350–1000 nm range. It is used for measurements of radiances at various viewing and azimuth angles in the FOV and estimation of radiance uncertainties in the hyperspectral mode.
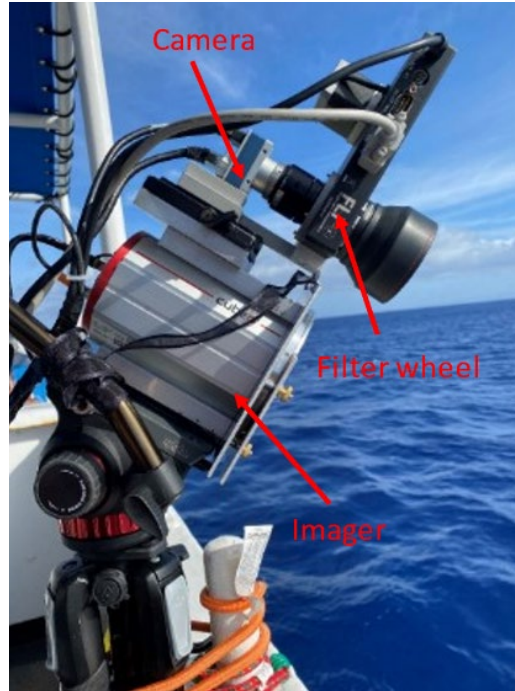
Figure 14. Snapshot hyperspectral imager with polarization camera on the ship.

- Polarization camera

Recently released Sony image polarization sensor with 2464 (H) × 2056 (V) pixels where each 2×2 pixel area consists of four subpixels that are equipped with polarizers oriented at 0°, 90°, 45° and -45°, respectively, was integrated by the Teledyne DALSA into M2450 camera and calibrated at CCNY. In our implementation it is combined with a lens and a filter wheel (Finger Lakes Instrumentation, NY) containing five color band-pass filters (AVR Optics, NY) with rectangular transmission spectra at the following center wavelengths (bandwidths) 442 (42), 494 (41), 550 (32), 655(40), 684 (24) nm and one window without filter and measurements in the panchromatic mode. The camera and lens provide a rectangular FOV (HFOV × VFOV = 29.2° × 38.4°) similar to the FOV of the imager. Typical integration time was 2 ms for water measurements, 0.7 ms for sky measurements, and 0.05 ms for white plaque measurements. Videos of the water surface were acquired with a typical frame rate of about 30–40 frames/second and 8-bit digitization, and standalone images were acquired with 8- and 12-bit digitization. The user interface provided by the manufacturer was integrated with the filter wheel interface to allow for the automatic acquisition of videos and images of polarization components. These images and videos were then reprocessed to get images and videos of Stokes vector components, the DoLP, and the angle of linear polarization (AoLP), which are further used in the analysis (Malinowski et al., 2023).

Polarimetric measurements provide important information in the characterization of ocean wave slopes (Zappa et al., 2008) and analysis of their variability in different open ocean and coastal areas as a function of wind speed in comparison with the Cox-Munk model (Cox and Munk, 1954), which is in the atmospheric correction model.

4.3.3 Example data and comparisons

Examples of comparison of measurements by GER, MOBY, new MOBY, and OC satellites are shown in Figure 15. GER spectra were adjusted to have $R_{rs} = 0$ at 750 nm. As typical for the open ocean, most of the data match well with satellite data and, in this cruise, also with the relevant sets of the MOBY data.

An example of imager data from one of the stations is shown in Figure 16.

Examples of images from the polarization camera are presented in Figure 17, showing the distribution of the Stokes vector components, I, Q/I, U/I, and the degree of polarization in the field of view.

Examples of the estimation of wave slope variances using polarimetric sensing with modified Zappa et al. (2008) algorithm at three different bands and comparison them with Cox and Munk (1954) variances are shown in Figure 18. Slope variances obviously should not depend on the band and such small dependence is visible in Figure 18 with variances close to Cox-Munk variances.
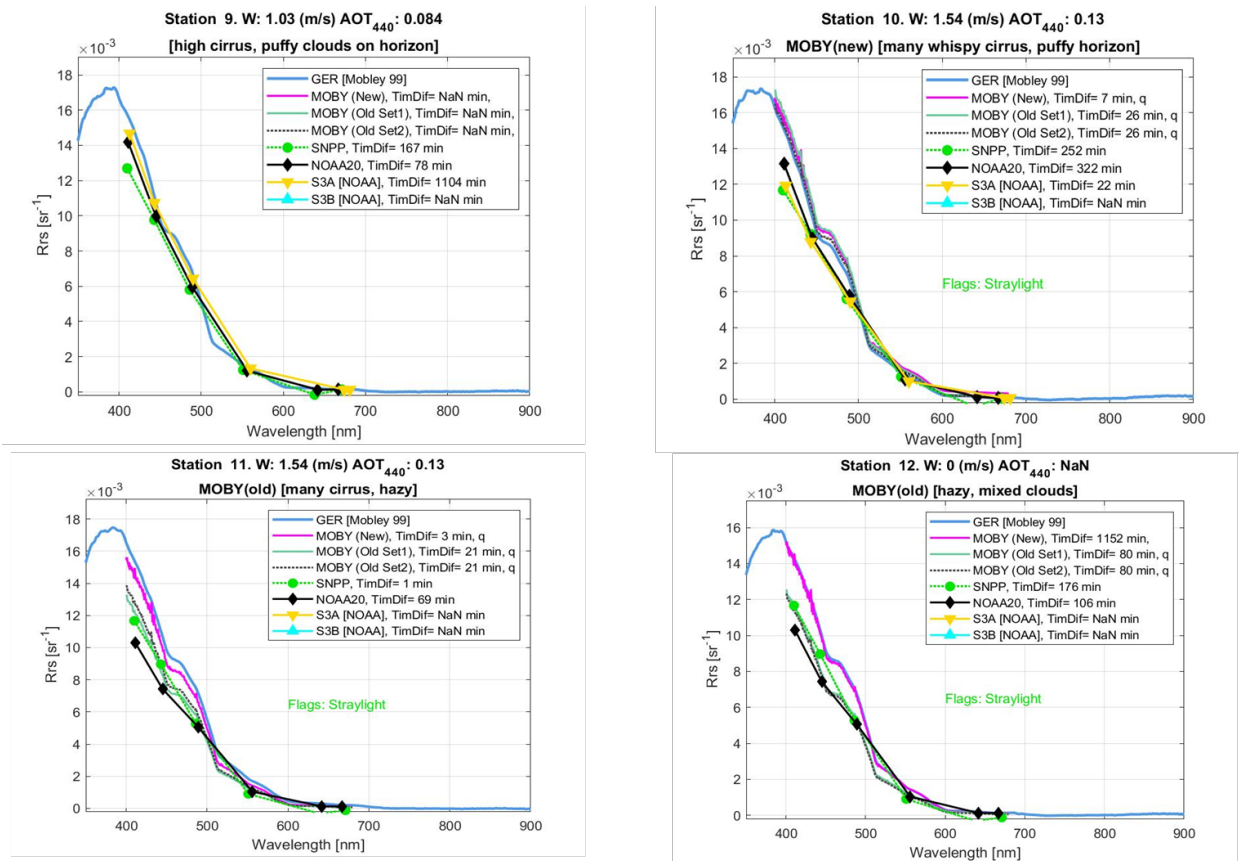
Figure 15. Comparison of measured spectra by GER with different MOBY and satellite data for several stations.
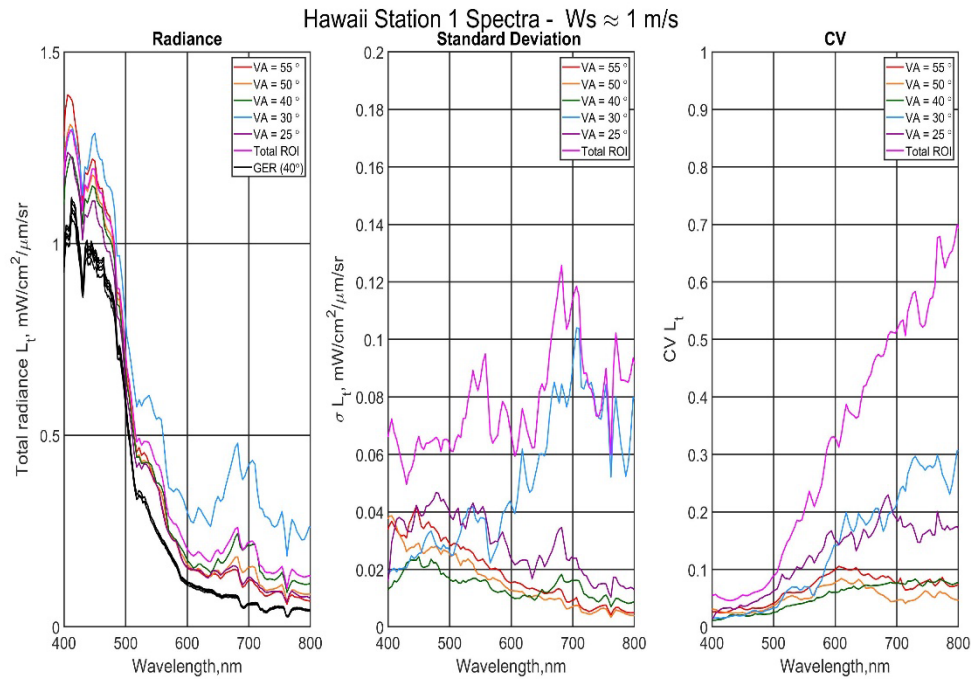
Figure 16. Data from the hyperspectral imager: above water spectral radiances at viewing angles 25–35° compared with GER spectra (left), radiances uncertainties (center), CV (right).
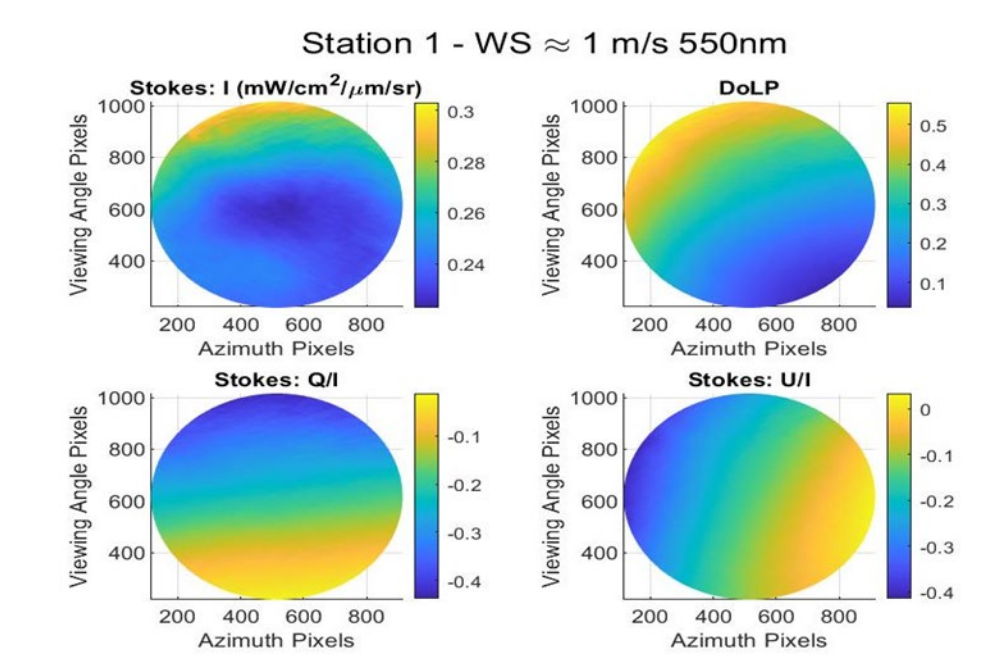
Figure 17. Example of the images from the polarization camera at Station 1.
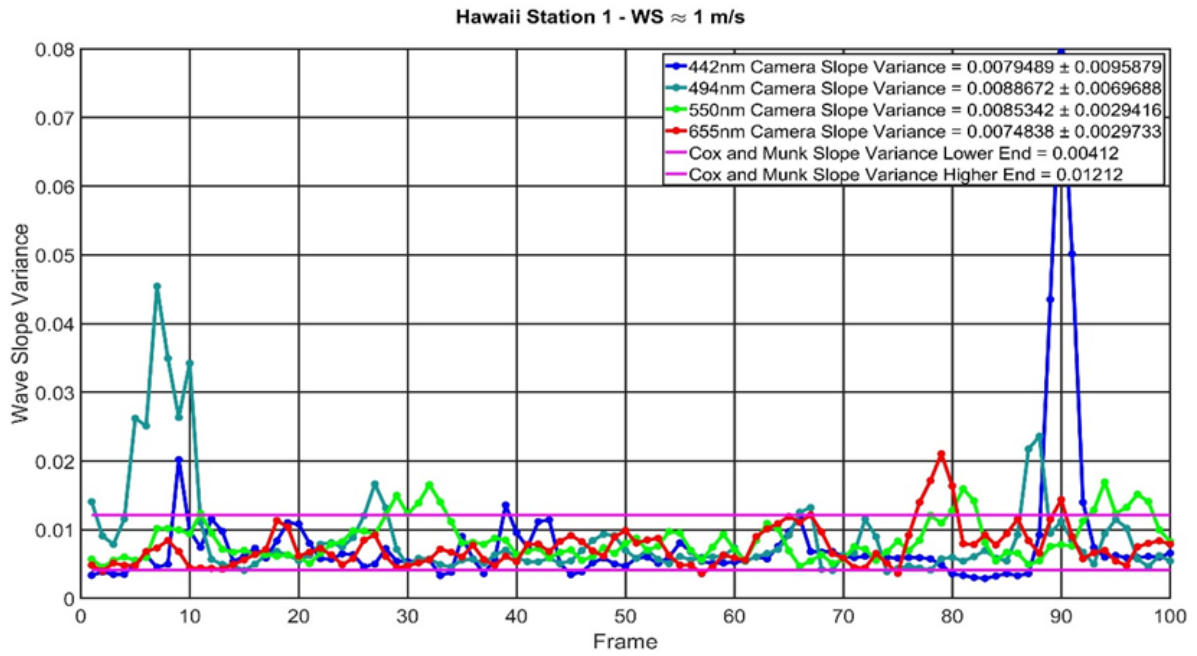
Figure 18. Estimation of wave slope variances using polarimetric sensing at Station 1.

4.4 LDEO team – Joaquim I. Goes, Jinghui Wu, and Helga do Rosario Gomes

The LDEO team undertook high-resolution measurements of chlorophyll, phytoplankton functional types, phytoplankton size classes, and phytoplankton photosynthetic efficiencies in near-surface (~5 m) seawater samples that were pumped continuously through the ship's uncontaminated flow-through seawater system. Additionally, samples from the three depths were filtered for Chl-a analysis in a Trilogy Fluorometer.

4.4.1 Discrete samples

Water samples were collected from a total of 24 stations along the cruise track. At each station, seawater samples were obtained from 3 depths in the water column for microscopic analysis of phytoplankton community composition and sizes.

    i.   Counting, imaging, and size estimations of phytoplankton and other detrital particles using a FlowCAM (Fluid Imaging Technologies, Inc.) (Jenkins et al., 2016).

    ii.   Fluorescence-based estimates of Chl-a (Holm-Hansen and Riemann, 1978b).

4.4.2 Underway flow-through measurements

Between stations, a suite of three instruments, an Automated Laser Fluorometer (ALF), a FlowCAM, and a Fluorescence Induction and Response (FIRe) were connected to the ship's seawater flow-through system (Jenkins et al., 2016) to make continuous measurements as follows:

    i.   ALF measurements of phytoplankton groups

The ALF combines high-resolution spectral measurements of blue (405 nm) and green (532 nm) laser-stimulated fluorescence with spectral deconvolution techniques to quantify the following:

- Fluorescence of Chl-a (peak at 679 nm).

- Three phycobilipigment types: Phycoerythrin-1 (PE-1; peak at 565 nm), Phycoerythrin-2 (PE-2; peak 578 nm), and Phycoerythrin-3 (PE-3; peak at 590 nm).

- CDOM (peak at 508 nm).

- F_v/F_m.

All fluorescence values obtained are normalized to the Raman spectra of seawater and generally expressed as relative fluorescence units (RFU), whereas F_v/F_m is unitless. PE-1 type pigments are associated with blue water or oligotrophic cyanobacteria with high phycourobilin/phycoerythrobilin (PUB/PEB) ratios, PE-2 type phytoplankton with low PUB/PEB ratios are generally associated with green water cyanobacteria that usually thrive in coastal mesohaline waters, and PE-3 attributable to eukaryotic photoautotrophic cryptophytes (Chekalyuk and Hafez, 2008; Chekalyuk et al., 2012; Goes et al., 2014b). RFU values for Chl-a can be converted into mg m^{-3} Chl-a values using least-square regressions of acetone or HPLC-measured Chl-a with RFU values for Chl-a measured in an ALF.

    ii.   FlowCAM-based phytoplankton identification, cell counts, and cell sizes

The FlowCAM particle imaging system used for this cruise was equipped with a 4X objective (UPlan FLN, Olympus®) and a 300 μm FOV flow cell. The system was hooked to the ship's seawater flow-through system to obtain continuous measurements of phytoplankton functional types, detrital particles, and particle size distribution of both phytoplankton and detrital particles. The 4X objective and the 300 μm FOV flow cell combination helped ensure that the liquid passing through the flow cell was entirely encompassed within the camera's field of view. All images captured by the FlowCAM will be classified to the genus level using the Visual Spreadsheet program (v. 2.2.2, Fluid Imaging) (Goes et al., 2014a; Goes et al., 2014b; Jenkins et al., 2016).
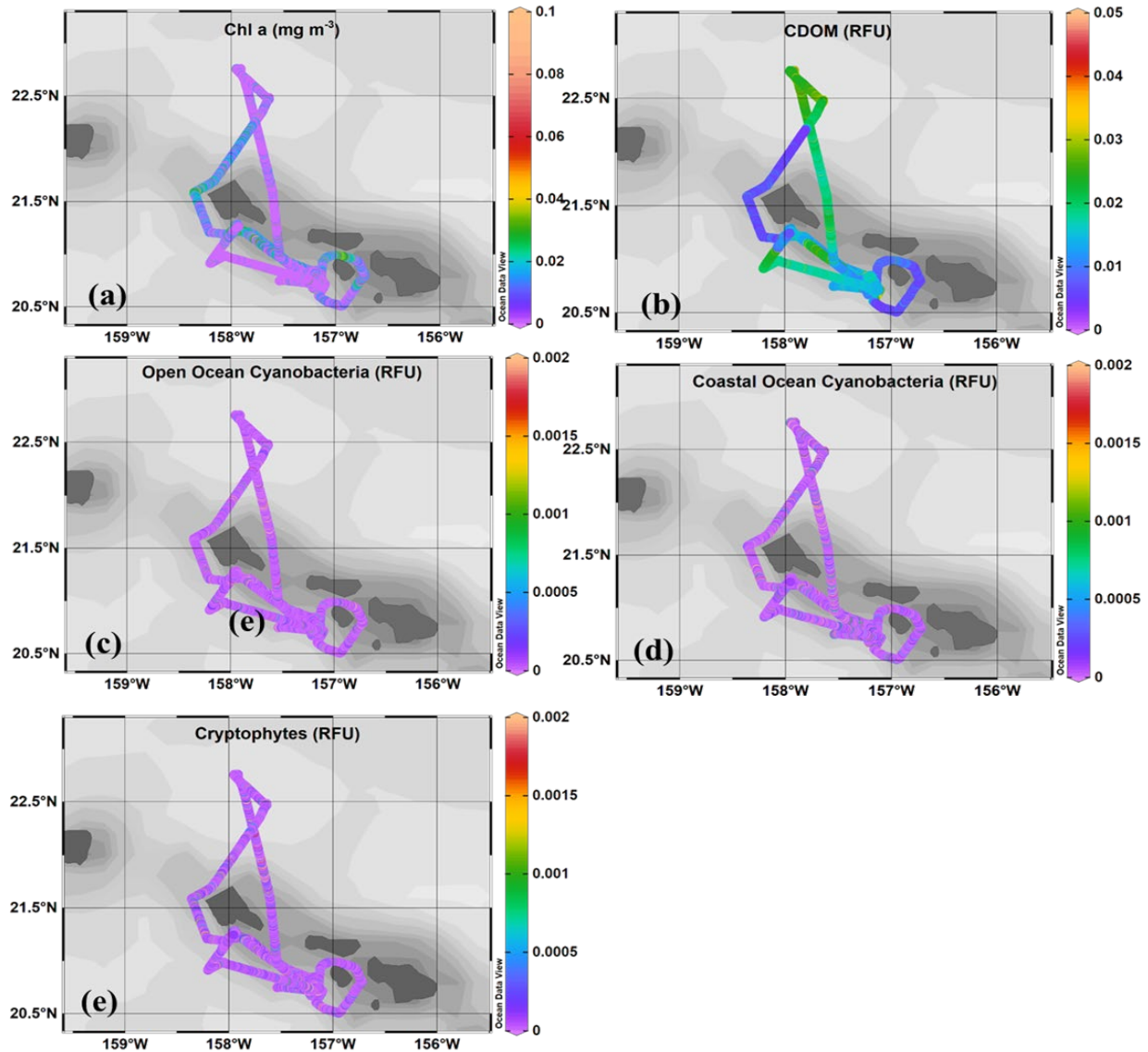
Figure 19. ALF derived a) Chl-a, b) CDOM, c) Open-Ocean Cyanobacteria, d) Coastal-Ocean Cyanobacteria, and e) Cryptophytes

iii. Fluorescence Induction and Relaxation (FIRe) measurements of photosynthetic competency

The FIRe instrument used during the cruise provides a comprehensive suite of photosynthetic and physiological characteristics of photosynthetic organisms (Bibby et al., 2008; Gorbunov and Falkowski, 2004). This technique provides a set of parameters that characterize photosynthetic light-harvesting processes, photochemistry in PSII (σ_{PSII}), phytoplankton variable fluorescence (*Fv/Fm*), and the photosynthetic ETR. All optical measurements by the FIRe are sensitive, fast, non-destructive, can be done in real-time and in situ, and can provide an instant measure of the photosynthetic efficiency of the cells (Wei et al., 2022b).

The use of these three instruments in tandem allowed for continuous in-water measurements of phytoplankton community composition, phytoplankton size, phycobilipigment types, and photosynthetic efficiency of phytoplankton along the cruise track. With the exception of a few breaks during stations and for reconditioning, the instruments were operated over the entire cruise track, providing several thousand fluorescence-based measurements of Chl-a, CDOM, PE-1, PE-2, PE-3, F_v/F_m, and σ_{PSII}, p (a measure of electron transport between the PSII and PSI. Continuous flow-through measurements of phytoplankton species distribution and cell size distribution along the cruise track will provide useful information for interpreting the optical measurements for phytoplankton functional types (PFTs) over the study area.

Preliminary data obtained with the flow-through instrumentation presented here allow us to obtain a synoptic picture of the distribution of phytoplankton biomass, CDOM, and community composition during the cruise (Figure 19a-e).

Chl-a concentrations were extremely low throughout the area transected by the ship, reflecting the highly oligotrophic nature of these waters. Chl-a concentrations barely exceeded 0.1 mg m^{-3}, the highest values being recorded in the channel between Lanai and Molokai (Figure 19a).

CDOM concentrations measured with the ALF were low but were clearly higher north, south, and west of Oahu Island. CDOM concentrations were lowest west of Oahu and around Yanai islands (Figure 19b)

The most abundant form of phytoplankton visible in the FlowCAM data were small round cells, presumably the cyanobacteria *Synechococcus* sp. These organisms can fix atmospheric nitrogen, and on account of their small size and large surface area to volume ratio, they can utilize small essential inorganic nutrients like phosphate when at low concentrations. The concentrations of three major groups (Open-Ocean Cyanobacteria, Coastal-Ocean Cyanobacteria, and Cryptophytes) that could be discriminated by the ALF were also very low (Figure 19c-e), and no single group dominated along the entire cruise track.

The maximum quantum yield of photosynthesis (Fv/Fm) obtained along the cruise track using the FIRe barely exceeded 0.4 (Figure 20a), an indication of the poor physiological health of the cells. This low quantum yield of photosynthesis can be linked to the poor nutrient concentrations in seawater.

Sigma-PSII (A^2) is a measure of the functional absorption cross-section of the cells. This parameter is a product of the optical absorption cross-section of PSII (i.e., the physical size of the PSII unit) and quantum yield of photochemistry in PSII and is reflective of the photo-physiological health of the cells. Higher values of sigma-PSII were clearly associated with waters north of Lanai Island

and south of Oahu Island, where the biomass and the quantum yield of the cells were also higher (Figure 20a-b).

The connectivity factor, p, defines the excitation energy transfer between individual photosynthetic units of PSII. This parameter is determined from the shape of the fluorescence induction curve and is also an important indication of trace-metal and other inorganic nutrient limitations. The values of p were higher south of Oahu Island and north of Lanai Island, corresponding to the high biomass regions obtained using the ALFA.
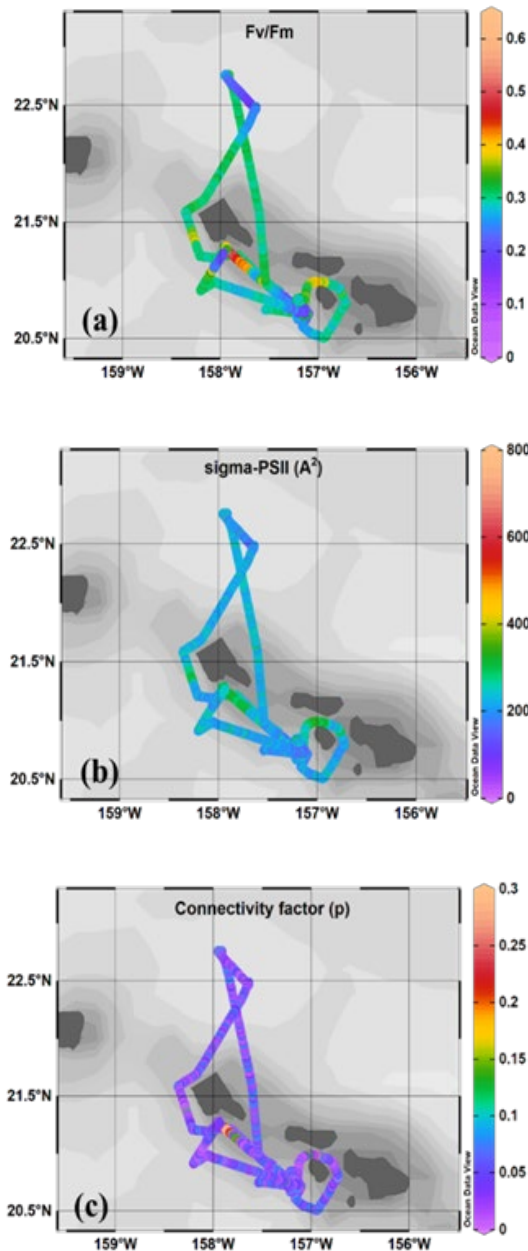
Figure 20. FIRe derived a) Fv/Fm, b) CDOM, c) Open Ocean Cyanobacteria, d) Coastal Ocean Cyanobacteria and e) Cryptophytes

4.5 USF team – Chuanmin Hu, Jennifer Cannizzaro, David English, Jing Shi, and Yao Yao

Three general types of measurements were made by individuals from the USF Optical Oceanography Lab during the cruise. The spectral absorption of particulate and dissolved material in discrete water samples was determined by analysis of water filtrations made during the cruise. The sea surface's remote sensing reflectance was determined from sequences of above-water measurements using a handheld spectroradiometer. A HyperPro-II radiometry system was also profiled through near-surface depths at each station to collect in-water radiometric profiles that can be used to estimate the remote sensing reflectance or normalized water-leaving radiance.

4.5.1 Spectral absorption and chlorophyll-a concentration

Shortly after water collection using the CTD rosette, a subset of water samples was filtered through a glass fiber filter (Whatman® GF/F) to allow later spectral measurements of the light absorption by particles in the water. A portion of the filtrate was further filtered through a 0.2 μm nylon membrane filter and reserved for shore-based measurement of the spectral absorption of dissolved material, $a_g(\lambda)$, in these water samples. The shore-based extraction of the particulate pigments allows the separation of the total particulate absorption, $a_p(\lambda)$, into a living or pigmented fraction, $a_{ph}(\lambda)$, and detrital fraction, $a_d(\lambda)$ (Kishino et al., 1985). The extraction of the pigments also allows a fluorometric determination of the Chl-a concentration (Holm-Hansen and Riemann, 1978a; Welschmeyer, 1994).

The Chl-a samples were processed using a Turner Trilogy fluorometer and as well as a Turner Designs 10-AU-005 fluorometer to verify the consistency of the results with samples processed for the JPSS VIIRS Ocean Color Cal/Val cruises that occurred before 2021. The particulate absorption measurements were made using a Perkin Elmer Lambda 850+ spectrophotometer.

The CTD sampling rosette was deployed in the relatively clear water found offshore of the Hawaiian Islands at 19 stations (Table 5Table 5. A summary of light absorption water sample times, types, and locations. All samples were collected from the CTD rosette bottles. A "●" indicates sample collection. The surface samples were collected at ~3 m depth.). In addition to the near-surface water samples, samples taken near the Chl-a maxima were also analyzed. There were 19 samples collected from surface waters and 19 from waters located at depths greater than 76 m. The Chl-a concentrations ranged from 0.04 to >0.57 mg m^{-3}. The absorption of both particulates and CDOM from the surface waters was consistently less than that of the deeper Chl-a maxima samples. Example spectral absorptions from the SE22-01 water samples are shown in Figure 21.

4.5.2 Above-water remote sensing reflectance

Above-water $R_{rs}(\lambda)$ was collected at 22 of the SE22-01 stations using a Spectra Vista Corp. (SVC) HR-512i spectroradiometer, though cloudy conditions diminished measurement reliability at four stations. The $R_{rs}(\lambda)$ estimate for each station is derived from multiple measurements of radiance from the water's surface, the sky, and a white-reference reflectance plaque (Carder and Steward, 1985; Mueller et al., 2003a) and incorporates a correction for reflected skylight (Mobley, 1999). The instrument had a 4° FOV as determined by the HR512i's fore-optic lens. The calibrated white reference reflectance plaque was set on a level platform near the ship's bow. The HR-512i viewed the sea surface and sky with viewing angles between 35° to 40° from nadir and zenith (θ_w and θ_s), respectively. The θ_w angle is recorded by the HR-512i for each measurement and was used in estimating the water's skylight reflectance value during the computation of the $R_{rs}(\lambda)$ estimates.
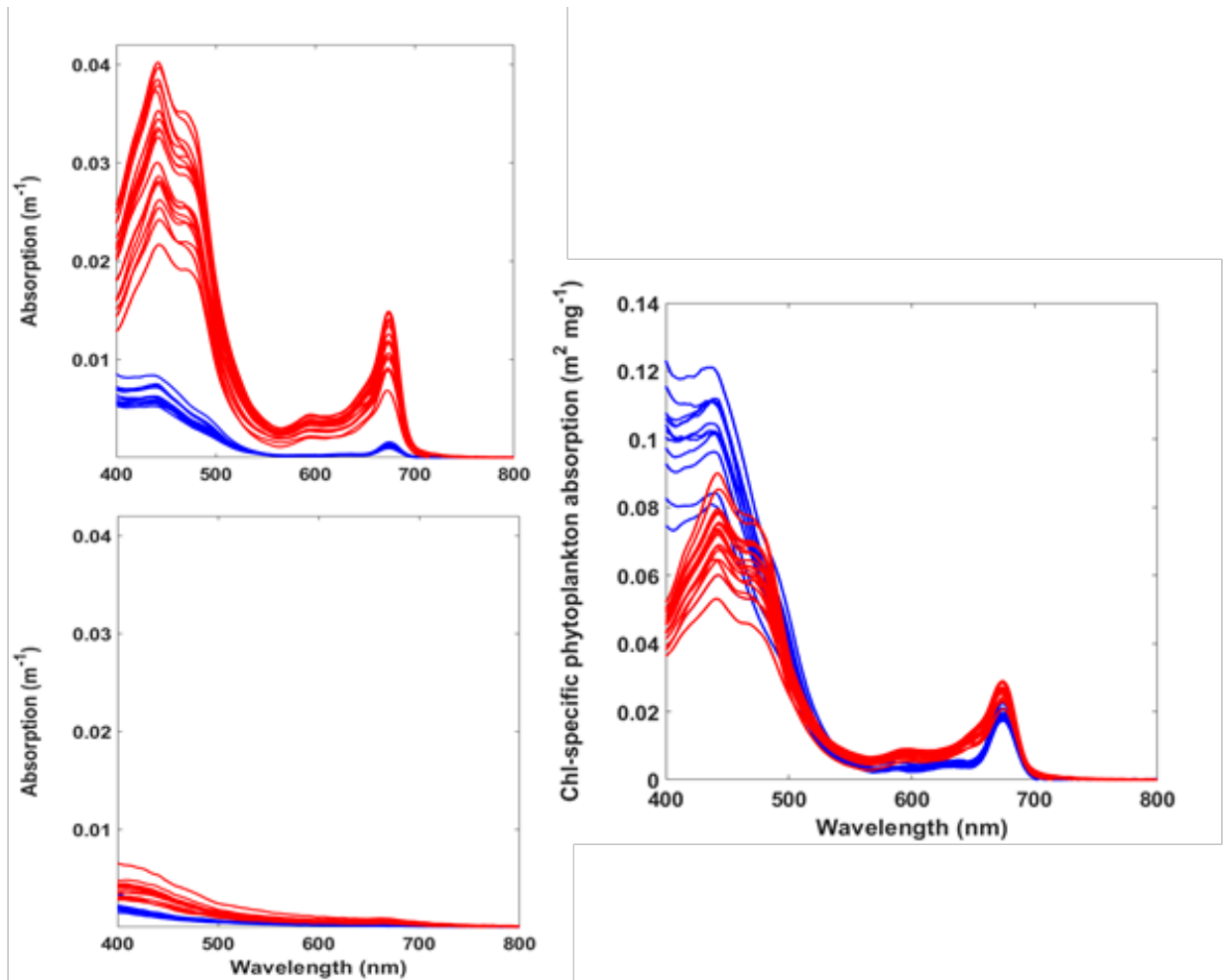
Figure 21. Spectral light absorption coefficients for phytoplankton pigments (top-left), non-pigmented particulate matter (i.e., detritus, bottom-left), and the chlorophyll-specific phytoplankton pigment absorption ($a_{ph}^{*}(\lambda)$, right panel). Values for near-surface samples are shown in blue, and those for deep-water samples are in red.

Table 6 shows the measurement times and locations of the above-water $R_{rs}(\lambda)$ and HyperPro-II stations. The above-water $R_{rs}(\lambda)$ estimates for all the stations (Figure 22) present a spectral shape that is typical for oligotrophic waters, as expected for offshore waters near Hawaii. The above-water $R_{rs}(\lambda)$ at VIIRS wavelengths showed good agreement with the 3×3 pixel medians at the measurement locations and times from both VIIRS/SNPP and VIIRS/NOAA-20 data (with quality control flags applied, data not shown).

Table 5. A summary of light absorption water sample times, types, and locations. All samples were collected from the CTD rosette bottles. A "●" indicates sample collection. The surface samples were collected at ~3 m depth.

Station	Sample time (UTC)	Latitude (°)	Longitude (°)	Surface sample	Subsurface sample	Subsurface depth (m)
1	3/9/2022 20:04	20.816	-157.189	●	●	110
2	3/10/2022 03:08	20.810	-157.173	●	●	97
3	3/11/2022 02:40	20.706	-157.143	●	●	103
4	3/11/2022 18:59	20.706	-157.143	●	●	114
5	3/12/2022 00:46	20.820	-157.180	●	●	100
6	3/12/2022 18:57	22.753	-157.927	●	●	130
7	3/13/2022 02:04	22.475	-157.640	●	●	117
8	3/13/2022 23:39	21.218	-158.460	●	●	121
9	3/14/2022 03:27	21.214	-158.620	●	●	120
10	3/14/2022 19:00	20.733	-157.137	●	●	82
11	3/14/2022 23:57	20.830	-157.180	●	●	103
12	3/15/2022 03:21	20.832	-157.186	●	●	101
13	3/15/2022 19:02	20.840	-157.204	●	●	76
14	3/16/2022 01:33	20.728	-157.139	●	●	85
15		20.727	-157.132			
16		20.733	-157.135			
17	3/16/2022 20:20	20.726	-157.146	●	●	91
18	3/17/2022 01:24	20.725	-157.141	●	●	98
19		20.735	-157.139			
20	3/17/2022 18:54	20.836	-157.203	●	●	91
21	3/17/2022 23:43	20.726	-157.151	●	●	81
22		20.732	-157.140			
23	3/18/2022 19:33	21.110	-158.061	●	●	124

Table 6. A summary of stations for above-water $R_{rs}(\lambda)$ and HyperPro-II profile measurements. The above water $R_{rs}(\lambda)$ and HyperPro-II measurements were usually conducted within 10 minutes of each other.

Station	Sample time (UTC)	Latitude (°)	Longitude (°)	above-water	HyperPro-II
1	3/9/2022 22:41	20.819	-157.187	Yes	Yes
2	3/10/2022 01:22	20.808	-157.185	Yes	Yes
3	3/11/2022 00:42	20.706	-157.144	Yes	Yes
4	3/11/2022 20:18	20.719	-157.142	Yes	Yes
5	3/11/2022 22:58	20.816	-157.182	Yes	Yes
6	3/12/2022 20:35	22.756	-157.933	Yes	Yes
7	3/13/2022 00:29	22.472	-157.64	Yes	Yes
8	3/13/2022 22:28	21.217	-158.457	Yes	Yes
9	3/14/2022 01:54	21.212	-158.62	Yes	Yes
10	3/14/2022 20:33	20.732	-157.136	Yes	Yes
11	3/14/2022 22:15	20.827	-157.179	Yes	Yes
12	3/15/2022 01:34	20.835	-157.187	Yes	Yes
13	3/15/2022 20:33	20.841	-157.206	Yes	Yes
14	3/15/2022 22:35	20.73	-157.138	Yes	Yes
15	3/15/2022 23:51	20.722	-157.135	Yes	Yes
16	3/16/2022 02:42	20.717	-157.133	no	Yes
17	3/16/2022 21:49	20.727	-157.146	Yes	Yes
18	3/16/2022 23:06	20.725	-157.141	Yes	Yes
19	3/17/2022 02:43	20.737	-157.139	Yes	Yes
20	3/17/2022 20:24	20.836	-157.202	Yes	Yes
21	3/17/2022 21:56	20.729	-157.153	Yes	Yes
22	3/18/2022 01:23	20.732	-157.14	Yes	no
23	3/18/2022 20:50	21.11	-158.061	Yes	Yes
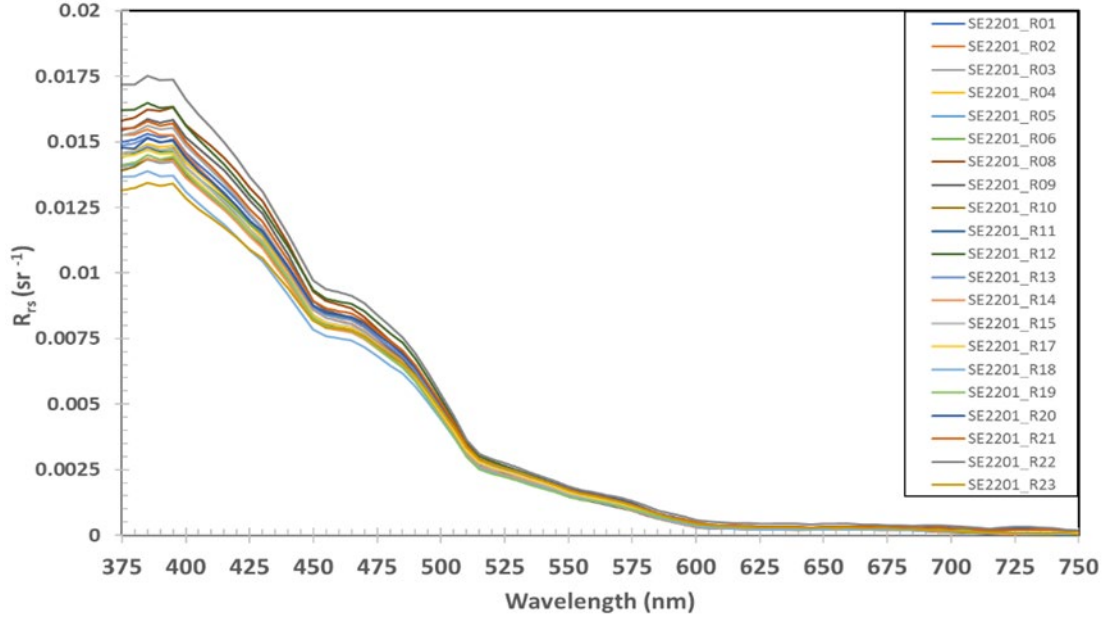
Figure 22. $R_{rs}(\lambda)$ derived from above-water HR-512i measurements during the cruise.

4.5.3 In-water radiometry

A Satlantic HyperPro-II II was deployed to collect vertical profiles of the near-surface water light field at 22 stations of SE22-01. The HyperPro-II profiler included not only $L_u(\lambda,z)$ and $E_d(\lambda,z)$ sensors but also sensors measuring pressure, temperature, conductivity, $b_b(660)$, and both Chl-a and CDOM fluorescence. The $L_u(\lambda,z)$ and $E_d(\lambda,z)$ measurements from multiple casts were used at each station to estimate radiance, irradiance, and reflectance (i.e., $L_w(\lambda,0^+)$ and $E_d(\lambda,0^+)$, $R_{rs}(\lambda)$, and $nL_w(\lambda)$) at the sea surface. USF's HyperPro-II profiler was deployed using the manufacturer's recommended protocol (Satlantic, 2003, 2004) in coordination with the other HyperPro-II profilers in use during the cruise. $R_{rs}(\lambda)$ estimates derived from the HyperPro-II profiles at each station are shown in Figure 23.

While the reliability of above-water R_{rs} measurements is decreased and the variability is increased when cloudy skies are present at the time of the measurements, a comparison of the above-water $R_{rs}(\lambda)$ estimates to those of the HyperPro-II profiler showed $R_{rs}(\lambda)$ with similar magnitudes and spectral shapes. Good agreement was observed between the estimates of $R_{rs}(\lambda)$ for several satellite wavebands (i.e., 410, 443, 486, and 551 nm) derived from HyperPro-II casts and from above-water HR512i measurements, as shown in Figure 24.
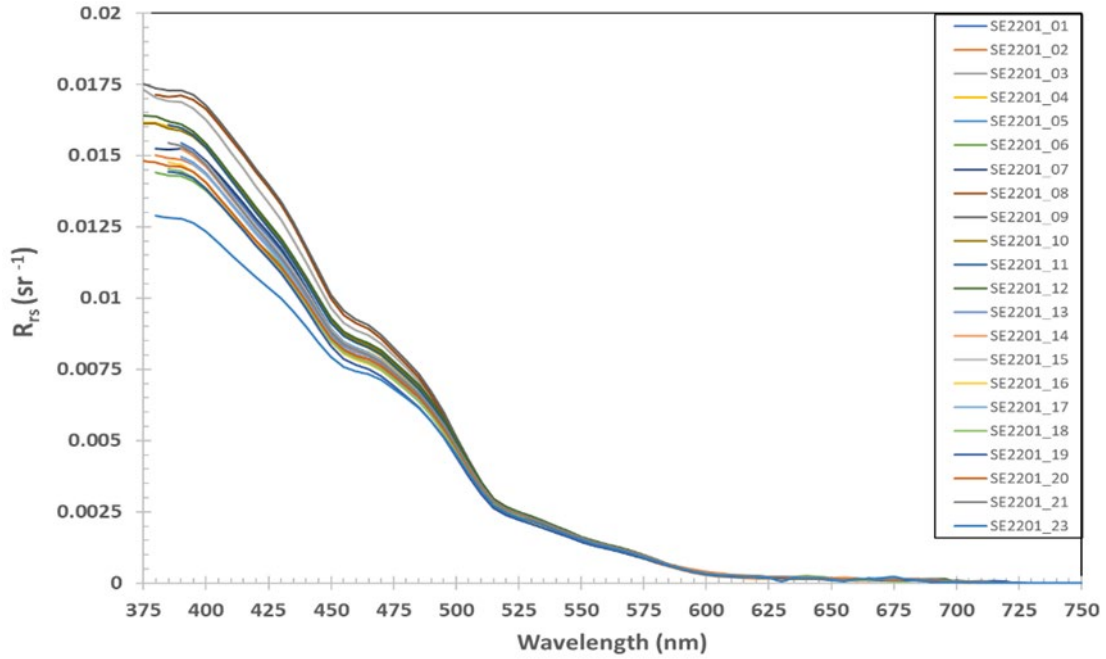
Figure 23. $R_{rs}(\lambda)$ estimated from HyperPro-II profiles during the cruise.
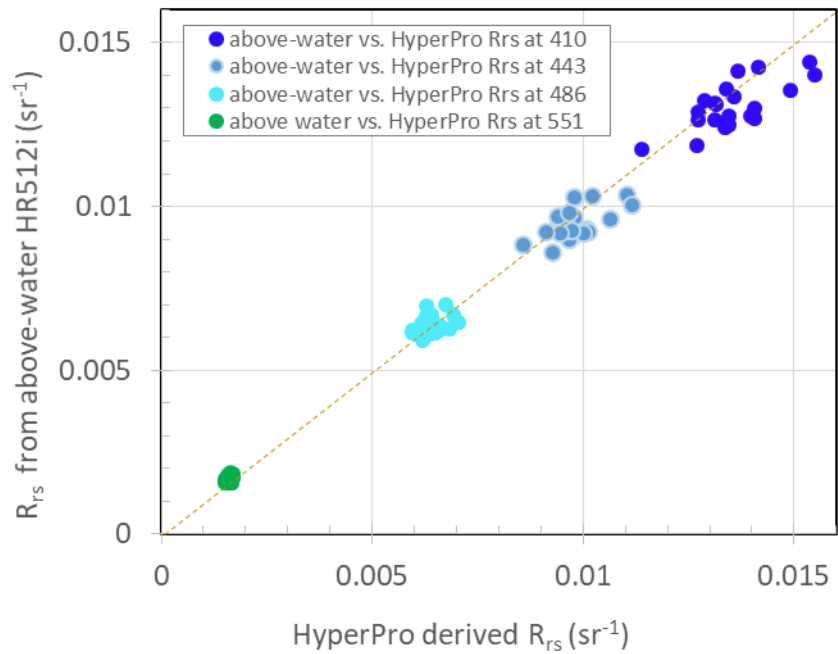
Figure 24. Comparison for several VIIRS satellite wavebands of R_{rs} derived from the HyperPro-II profiles and above-water HR512i R_{rs} measurements, including those with cloudy conditions or extreme solar zenith angles.

4.6 OSU team – Nick Tufillaro, Alexander Bailess, Adam Belmonte, Andrew Barnard, Jing Tan, and Robert Frouin

OSU participated in the 2022 Cal/Val cruise, measuring apparent optical properties on the waters surrounding Hawaii using a hyperspectral in-water profiler and a new hyperspectral sensor system (HyperNAV) configured to operate as a surface buoy. OSU's main objectives for this cruise were first to derive water-leaving radiances and reflectances from the in-water profilers for instrumental inter-comparison and ocean color product validation for VIIRS/SNPP and VIIRS/NOAA-20, and second, the deployment and testing of a new in-water hyperspectral sensor system, HyperNAV, which can be compared to current operational tools such as HyperPro-II in the buoy configuration (Barnard et al., 2018). OSU also tested a new software platform for logging and tracking the HyperNAV, called *Inlinino,* which was tested for compatibility with HyperNAV and HyperPro-II deployments, along with Satlantic's current logging platform, SatView (Haëntjens and Boss, 2020).

4.6.1 Apparent optical properties by profilers

OSU operated a series of hyperspectral ocean color sensors using the Satlantic HyperPro-II in the freefall profiler configuration. A downwelling irradiance sensor was mounted on a Grappa pole on the ship with other irradiance sensors to reduce stray light contamination from the vessel. An upwelling radiance sensor and a downwelling irradiance sensor were mounted directly onto the HyperPro-II system in the standard configuration to derive water-leaving radiances and reflectances. The HyperPro-II is also equipped with a WET Labs ECO Puck, measuring scattering at 470 nm and 700 nm and chlorophyll fluorescence at 470 nm and 695 nm.

The HyperPro-II was deployed overboard and kited away from the ship so that the shadow of the ship and other stray light effects from the vessel would not interfere with the optical measurements. As a rule of thumb, the HyperPro-II was kited at least 20m away from the hull. We ensured that the E_d sensor of the HyperPro-II was facing the sun to avoid self-shadowing during deployment. Weighting in the 'nose cone' is configured for the ambient density to allow for 'slop drop' at ~0.3 m/s for adequate data collection.

Data was collected using Satlantic's SatView, and Nils Haentjen's (University of Maine), *Inlinino*, which is available at: *https://github.com/OceanOptics/Inlinino*. Recent updates of *Inlinino* are compatible with the deployment of the HyperPro-II system, and we favored this User Interface (UI) to Satlantic's SatView. Post-processing was performed with Satlantic's ProSoft version 8.1.4 using protocols outlined by Oregon State University, available for download at: *http://aquahue.net/aquahue/papers/x_tec_hyperpro_processing.pdf*. Data was also processed with the NOAA protocols developed by M. Ondrusek. The equations used by ProSoft to derive the above water products such as,

$$R_L(0^+, \lambda) = \frac{L_w(0^+, \lambda)}{E_d(0^+, \lambda)} \tag{2}$$

where $E_d(0^+, \lambda)$ denotes the downwelling spectral irradiance measured just above the surface or extrapolated through the surface, and $L_w(0^+, \lambda)$ denotes the upwelling spectral radiance propagated through the surface. For E_s from the ship-based irradiance sensor, spectral bands are interpolated and matched to the in-water radiance sensor. Additional quantities, such as the normalized water-leaving radiance and remote sensing reflectance, are defined as in Mobley (1994).
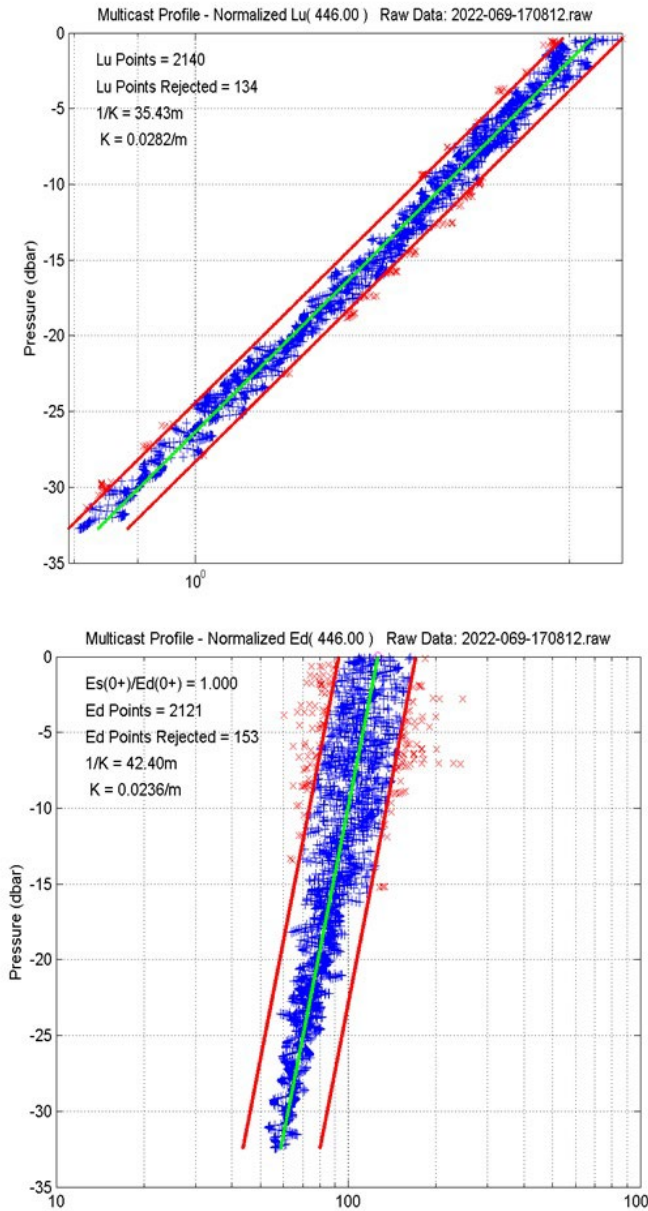
Figure 25. Examples of L_u and E_d profiles from the HyperPro-II for blue light (446 nm)

An example of the in-water L_u and E_s is shown in Figure 25 for 446 nm to give a sense of the error distribution for these waters in the North Pacific. The clarity is reflected in the first optical depth (42 m). These are particularly tight profiles due to the relative uniformity of the upper water column in the North Pacific Gyre. Figure 25 displays a high density of points at each depth, sometimes overlapping. This high density of measurements comes from several profiles (3–5) of the instrument for each 'cast'. This 'yo-yo' profiling allows for better surface reflectance values that allow us to average the effects of suboptimal tilt and wave focusing.

One example of the water-leaving radiance derived from the HyperPro-II profiler is shown in Figure 26 for the last day of the cruise.
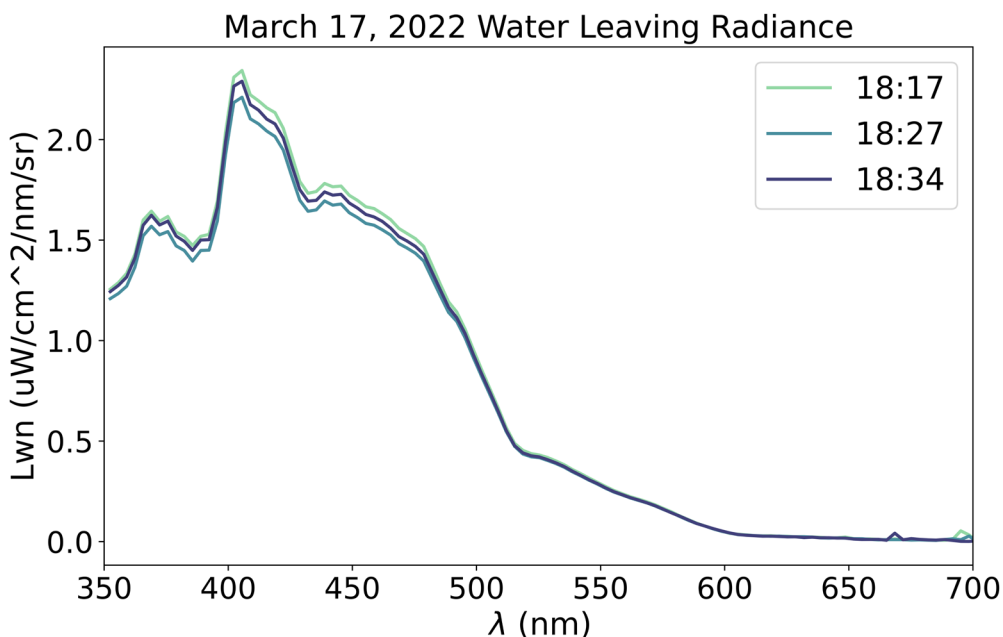
Figure 26. An example of water-leaving radiance derived from OSU HyperPro-II on March 17, 2022.

4.6.2 Apparent optical properties by surface buoys

OSU also spearheaded the deployment of a brand new state-of-the-art in-water radiometer, the HyperNAV. The HyperNAV system is being developed by SeaBird with support from NASA as part of the PACE program, which requires the use of new hyperspectral instruments for calibration and validation. The HyperNAV has a significantly enhanced spectral resolution (sample spacing ~0.4 nm/pixel, spectral resolution ~ 2 nm) compared to the HyperOCR sensors on the HyperPro-II (sample spacing ~3 nm/pixel, spectral resolution ~10 nm). This allows for the visualization of fine-scale features such as Fraunhofer lines, even in upwelling radiances. The HyperNAV is configured with two advanced independent L_u sensors with a nominal spectral range as specified by the PACE team requirements (350–900 nm). Each head is extended away from the main body

to avoid self-shading effects. In the buoy configuration, the HyperNAV sits at the surface with each radiance head ~10 cm below the surface to reduce uncertainties in the extrapolation of above-water products. The HyperNAV is slightly bigger than the HypePro-II models (Figure 27) and can be deployed simultaneously with HyperPros. On this cruise, the HyperNAV was deployed concurrently with two HyperPros with an SBA configuration, as described by Lee et al. (2019) and Wei et al. (2021b) and as shown in Figure 28.

To deploy the HyperNAV in a surface buoy configuration, a buoyant 'wing' is fitted to the frame, which allows the system to kite an adequate distance away from the vessel. The buoyancy is adjusted with stainless steel washers in the nose cone until each of the L_u heads is 10 cm below the surface. Dual L_u sensors on HyperNAV provide independent measurements of upwelling radiance at the surface, facilitating comparisons between the two radiance sensors for the effects of solar/platform shading as well as analyses of the wave-focusing effect. On this cruise, we performed several casts with the NRL and SFU HyperPros in the SBA configuration for comparison. The three best HyperNAV casts are shown below in Figure 29. To compare R_{rs} between concurrent HyperNAV and HyperPro casts, high-resolution E_s were modeled by Jing Tan and Robert Frouin (Scripps Institution of Oceanography, University of California San Diego) using ARTDECO. These models were validated with in situ HyperOCR irradiance measurements. Note the detail in the spectra of upwelling radiance compared to that of the HyperPro in Figure 30.

Figure 27. Comparison of HyperNAV (left) and HyperPro-II (right)

Figure 28. HyperNAV (front) in the surface buoy mode, with two HyperPro-IIs in the SBA configuration behind.
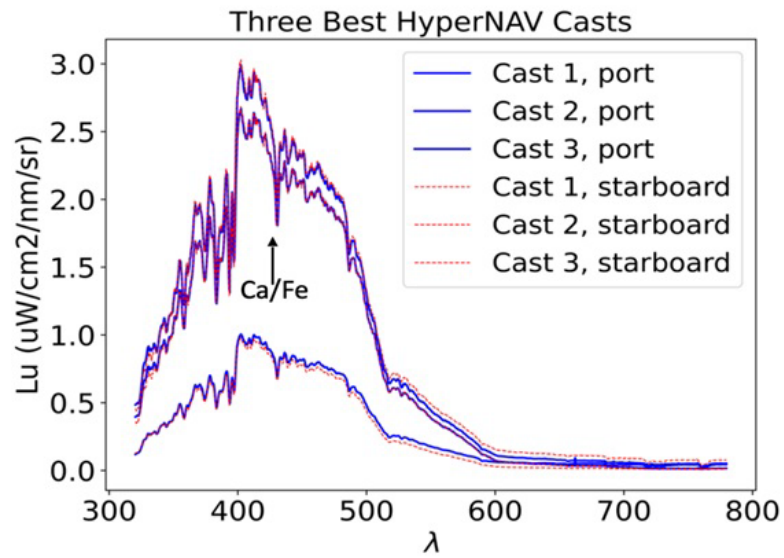
Figure 29. Example spectra of upwelling radiance (L_u) from the HyperNAV during the cruise. Note the Fraunhofer bands visible with this level of spectral resolution, for example, solar absorption of Calcium and Iron at ~430 nm.

As a reference, Table 7–Table 9 below provide a list of all OSU casts during the entire cruise period.

Table 7. Reference table for in-water profiler casts (stations 1–8) made by the OSU team in the cruise.

Station	Filename	2022 Julian Day	Local Time	Latitude	Longitude	Cast Type
1	2022-068-144253.raw	68	12:42	20.8232	-157.19283	yo-yo
1	2022-068-144322.raw	68	12:43	20.8232	-157.19283	yo-yo
1	2022-068-150143.raw	68	13:01	20.8232	-157.19283	yo-yo
1	2022-068-151345.raw	68	13:13	20.8232	-157.19283	yo-yo
2	2022-068-172423.raw	68	15:24	20.8081	-157.1798	yo-yo
2	2022-068-173300.raw	68	15:33	20.8081	-157.1798	yo-yo
2	2022-068-174456.raw	68	15:44	20.8081	-157.1798	yo-yo
3	2022-069-164450.raw	69	14:44	20.706233	-157.14357	yo-yo
3	2022-069-165618.raw	69	14:56	20.706233	-157.14357	yo-yo
3	2022-069-170812.raw	69	15:08	20.706233	-157.14357	yo-yo
4	2022-070-122008.raw	70	10:20	20.720967	-157.14343	yo-yo
4	2022-070-123656.raw	70	10:36	20.720967	-157.14343	yo-yo
4	2022-070-124634.raw	70	10:46	20.720967	-157.14343	yo-yo
5	2022-070-150055.raw	70	13:00	20.824867	-157.17857	yo-yo
5	2022-070-152204.raw	70	13:22	20.824867	-157.17857	yo-yo
5	2022-070-153604.raw	70	13:36	20.824867	-157.17857	yo-yo
6	2022-071-123753.raw	71	10:37	22.759025	-157.9394	yo-yo
6	2022-071-125055.raw	71	10:50	22.759025	-157.9394	yo-yo
6	2022-071-130128.raw	71	11:01	22.759025	-157.9394	yo-yo
7	2022-071-163124.raw	71	14:31	22.47415	157.64119	yo-yo
7	2022-071-165434.raw	71	14:54	22.47415	157.64119	yo-yo
8	2022-072-153026.raw	72	13:30	21.218371	158.45916	yo-yo
8	2022-072-153633.raw	72	13:36	21.218371	158.45916	yo-yo
8	2022-072-154337.raw	72	13:43	21.218371	158.45916	yo-yo
8	2022-072-154903.raw	72	13:49	21.218371	158.45916	yo-yo

Table 8. Reference table for in-water profiler casts (stations 9–17) made by the OSU team in the cruise.

Station	Filename	2022 Julian Day	Local Time	Latitude	Longitude	Cast Type
9	2022-072-185628.raw	72	16:56	21.213306	158.61977	yo-yo
9	2022-072-190143.raw	72	17:01	21.213306	158.61977	yo-yo
9	2022-072-191118.raw	72	17:11	21.213306	158.61977	yo-yo
10	2022-073-133647.raw	73	11:36	20.732917	157.13634	yo-yo
10	2022-073-134724.raw	73	11:47	20.732917	157.13634	yo-yo
10	2022-073-140515.raw	73	12:05	20.732917	157.13634	yo-yo
11	2022-073-151751.raw	73	13:17	20.828058	157.17946	yo-yo
11	2022-073-152611.raw	73	13:26	20.828058	157.17946	yo-yo
12	2022-073-183701.raw	73	16:37	20.837125	157.18796	yo-yo
12	2022-073-184412.raw	73	16:44	20.837125	157.18796	yo-yo
12	2022-073-184940.raw	73	16:49	20.837125	157.18796	yo-yo
12	2022-073-185445.raw	73	16:54	20.837125	157.18796	yo-yo
14	2022-074-133541.raw	74	11:35	20.8415	-157.20937	yo-yo
14	2022-074-134245.raw	74	11:42	20.8415	-157.20937	yo-yo
14	2022-074-135027.raw	74	11:50	20.8415	-157.20937	yo-yo
15	2022-074-152508.raw	74	13:25	20.7306	-157.1381	yo-yo
15	2022-074-153202.raw	74	13:32	20.7306	-157.1381	yo-yo
15	2022-074-153759.raw	74	13:37	20.7306	-157.1381	yo-yo
16	2022-074-165325.raw	74	14:53	20.724733	-157.13293	yo-yo
16	2022-074-165956.raw	74	14:59	20.724733	-157.13293	yo-yo
16	2022-074-170443.raw	74	15:04	20.724733	-157.13293	yo-yo
17	2022-074-194442.raw	74	17:44	20.718622	157.13207	yo-yo
17	2022-074-194903.raw	74	17:49	20.718622	157.13207	yo-yo
17	2022-074-195409.raw	74	17:54	20.718622	157.13207	yo-yo

Table 9. Reference table for in-water profiler casts (stations 18–24) made by the OSU team in the cruise.

Station	Filename	2022 Julian Day	Local Time	Latitude	Longitude	Cast Type
18	2022-075-145131.raw	75	12:51	20.7292	157.14824	yo-yo
18	2022-075-145729.raw	75	12:57	20.7292	157.14824	yo-yo
18	2022-075-150445.raw	75	13:04	20.7292	157.14824	yo-yo
19	2022-075-160825.raw	75	14:08	20.731728	157.14221	yo-yo
19	2022-075-161904.raw	75	14:19	20.731728	157.14221	yo-yo
19	2022-075-162759.raw	75	14:27	20.731728	157.14221	yo-yo
20	2022-075-194510.raw	75	17:45	20.739917	157.1372	yo-yo
20	2022-075-195151.raw	75	17:51	20.739917	157.1372	yo-yo
20	2022-075-195736.raw	75	17:57	20.739917	157.1372	yo-yo
21	2022-076-132645.raw	76	11:26	20.836267	157.20424	yo-yo
21	2022-076-133203.raw	76	11:32	20.836267	157.20424	yo-yo
21	2022-076-133915.raw	76	11:39	20.836267	157.20424	yo-yo
22	2022-076-145814.raw	76	12:58	20.730678	157.1538	yo-yo
22	2022-076-150349.raw	76	13:03	20.730678	157.1538	yo-yo
22	2022-076-150912.raw	76	13:09	20.730678	157.1538	yo-yo
23	2022-076-181520.raw	76	16:15	20.737944	157.13926	yo-yo
23	2022-076-181706.raw	76	16:17	20.737944	157.13926	yo-yo
23	2022-076-182747.raw	76	16:27	20.737944	157.13926	yo-yo
23	2022-076-183442.raw	76	16:34	20.737944	157.13926	yo-yo
23	2022-076-195201.raw	76	17:52	20.737944	157.13926	yo-yo
23	2022-076-195750.raw	76	17:57	20.737944	157.13926	yo-yo
23	2022-076-200147.raw	76	18:01	20.737944	157.13926	yo-yo
23	2022-076-210131.raw	76	19:01	20.737944	157.13926	yo-yo
24	2022-077-135225.raw	77	11:52	21.110733	158.06211	yo-yo
24	2022-077-135636.raw	77	11:56	21.110733	158.06211	yo-yo
24	2022-077-140159.raw	77	12:01	21.110733	158.06211	yo-yo
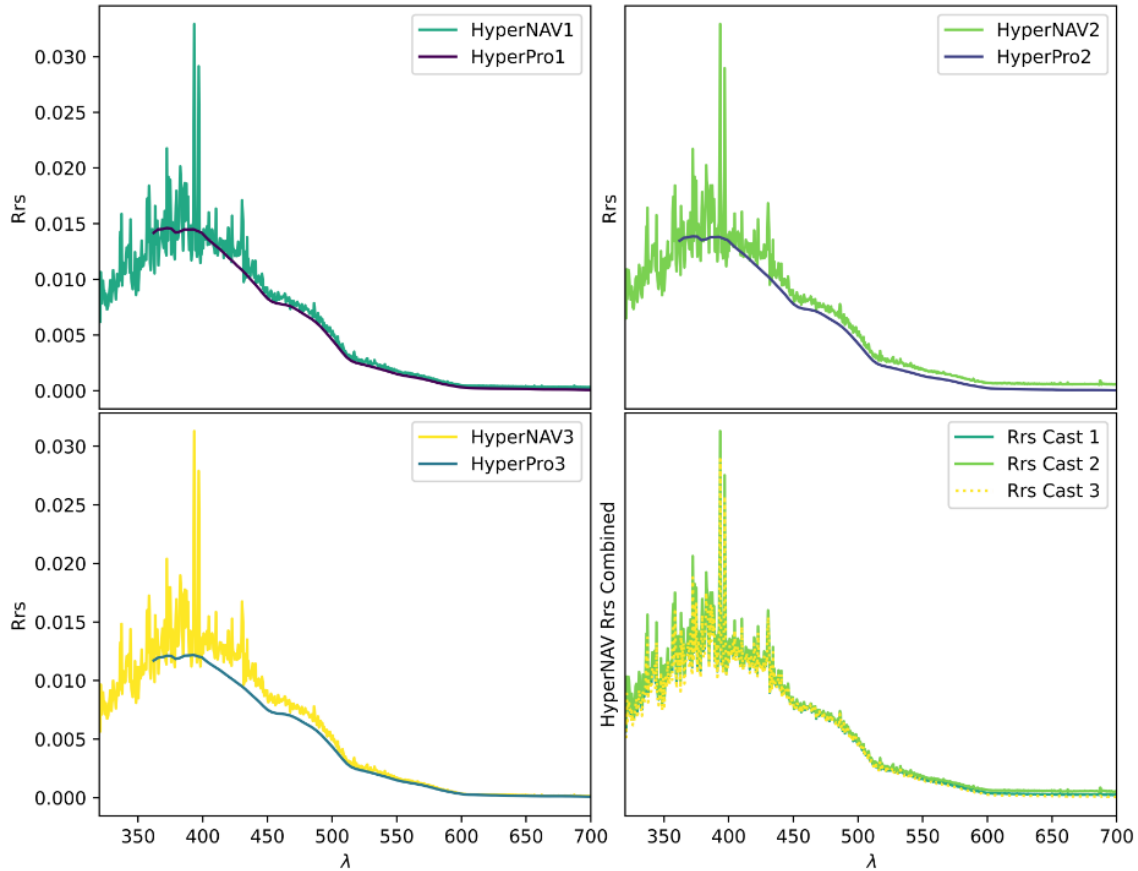
Figure 30. Comparison of $R_{rs}(\lambda)$ from concurrent HyperNAV and HyperPro casts. High-resolution $E_s(\lambda)$ for the derivation of reflectances was modeled by Jing Tan and Robert Frouin using ARTDECO. These models were validated with an in-situ HyperOCR $E_s(\lambda)$.

4.6.3 Summary

Reflectances and water leaving radiances were derived for all stations using data from the in-water profilers. The HyperNAV, a higher-resolution version of the HyperPro-II, was tested in the surface buoy configuration. We gathered data on the best methods for shipborne deployment and tested the logging software *Inlinino* for compatibility with both these in-water hyperspectral systems. Preliminary comparisons were performed on the HyperPro-II and HyperNAV upwelling radiances and remote sensing reflectance.

We continue to refine HyperPro-II to HyperNAV comparisons for continuity going forward with remote sensing products. Issues of spectral bandwidth, response, and matching, in conjunction with uncertainty analysis, are necessary to integrate data generated from both these systems.

4.7 NASA GSFC team – Antonio Mannino, Joaquín E. Chaves, Declan P. Farr, Scott A. Freeman, and Harrison D. Smith

4.7.1 NASA science objectives

The JPSS VIIRS 2022 campaign presented an opportunity to collect optical measurements concurrently with phytoplankton pigments and other biogeochemical parameters to support NASA's ocean color sensor validation. The objective of the NASA Ocean Ecology Laboratory Field Support Group (FSG) team was to contribute to the datasets of optical and biogeochemical data for use in sensor validation and algorithm development. NASA FSG is responsible for discrete Biogeochemical and optical property sampling and measuring apparent and inherent optical properties.

4.7.2 Cruise narrative

Joaquín Chaves, Declan Farr, Scott Freeman, and Harrison Smith traveled to Joint Base Pearl Harbor-Hickam (JBPHH), Honolulu, Hawaii, to begin mobilization on the NOAA Ship *Oscar Elton Sette* on March 4th, 2022. NASA FSG gear arrived at JBPHH on March 7th due to delays, and some mobilization was completed. Chief scientist Mike Ondrusek and the NOAA science party were delayed five days in joining due to positive COVID tests, and departure from JBPHH was delayed until March 8th. Science stations began at 09:00 local Hawaii time on March 9th. On March 10th, the ship crew retrieved a replacement Science Data Collection System (SDS) from JPBHH. On March 13th at 08:00, five of the six science party members, including chief scientist Mike Ondrusek, joined the ship after overnight transit back to JBPHH. The days at sea were spent around the MOBY system and the HOT station before the ship returned to port on Friday, March 18th, to begin demobilization.

4.7.3 Measurements of biogeochemical and optical properties

Water samples were collected from the CTD rosette Niskin bottles at two depths, near surface and within the subsurface chlorophyll maximum, at most cast stations. A subset of samples was collected from the underway clean science water system while on station. Filter or whole water sample duplicates collected were analyzed for the concentrations of photosynthetic phytoplankton pigments (PPig) using HPLC, SPM, POC, particulate nitrogen (PN), particulate inorganic carbon (PIC), dissolved organic carbon (DOC), and the spectral absorptions by particulates (a_p), and by CDOM (a_g). All filtration and cold sample preservation were conducted on board. Samples were filtered onboard under a low vacuum pressure (< 20 kPa). All filtration and onboard sample processing for POC, PN, PIC, and SPM filtration was conducted in a HEPA-filtered atmosphere to reduce contamination by foreign particles. Samples were transported to NASA-GSFC for further analysis. The summary of sample replicates collected for each parameter is presented in Table 10. Analytical results for the parameters analyzed thus far are presented in Figure 31–Figure 34.

Table 10. Discrete optical and biogeochemical sample replicates collected during the field campaign.

Parameter	Number of samples
a_p	56
a_g	30
PPig	75
DOC	71
POC	106*
PIC	40*
SPM	30*
Total	333

*Includes blanks
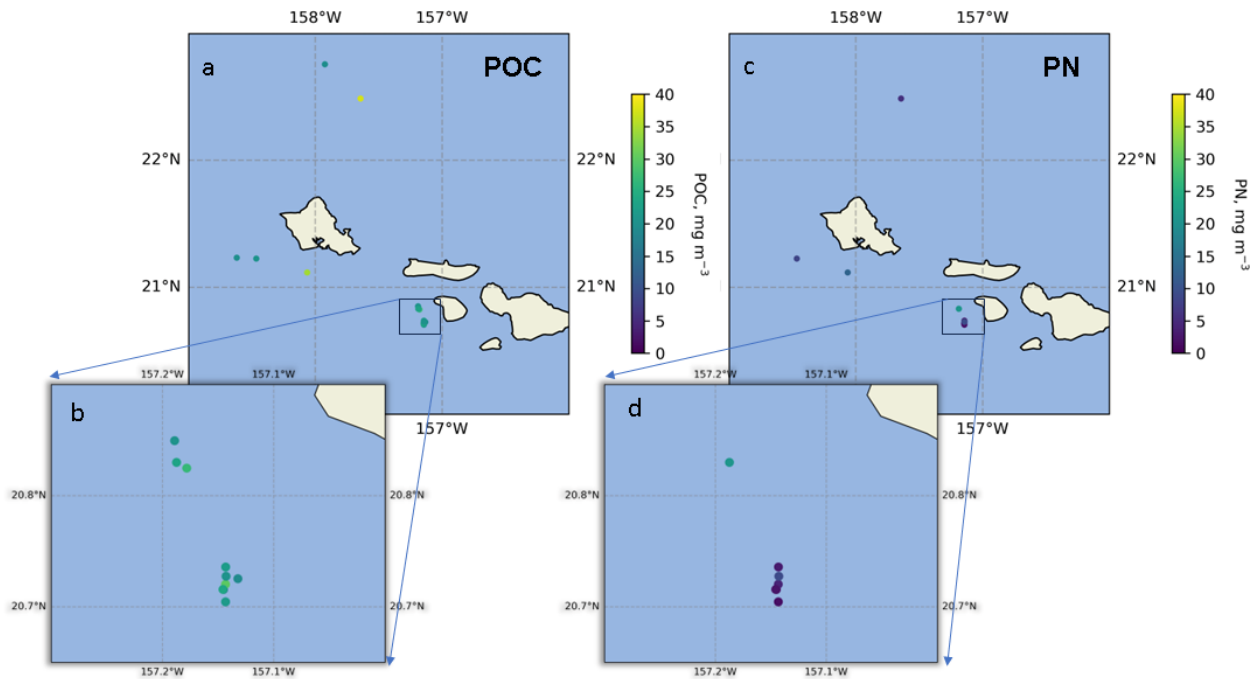
Figure 31. Concentration of (a, b) particulate organic carbon (POC), and (c, d) particulate nitrogen (PN) for near-surface samples collected during the field campaign.
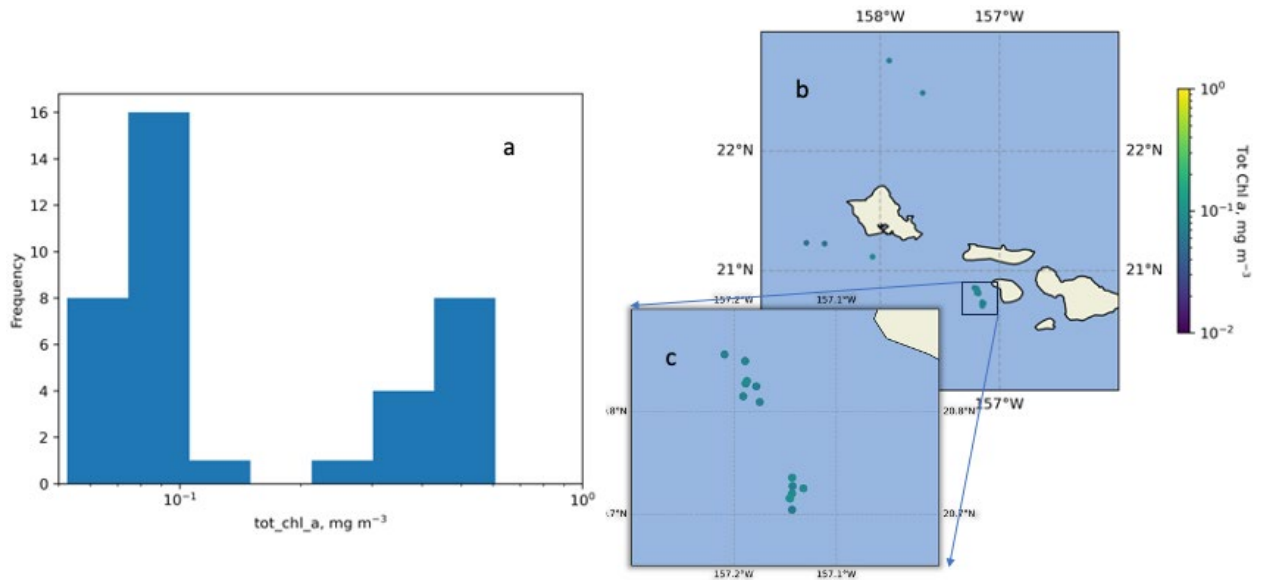
Figure 32. (a) Histogram of the concentration of total chlorophyll *a* analyzed by HPLC (TChla) for all samples, and (b, c) TChla for near-surface samples collected during the field campaign.
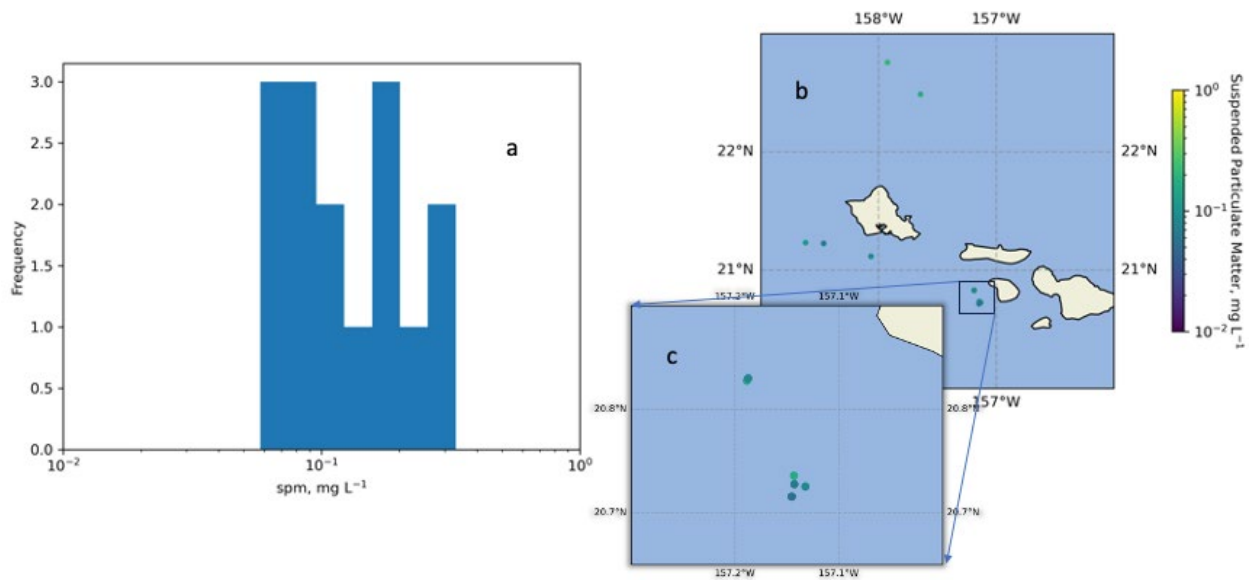
Figure 33. (a) Histogram of the concentration suspended particulate matter (SPM) for all samples, and (b, c) SPM for near-surface samples collected during the field campaign.
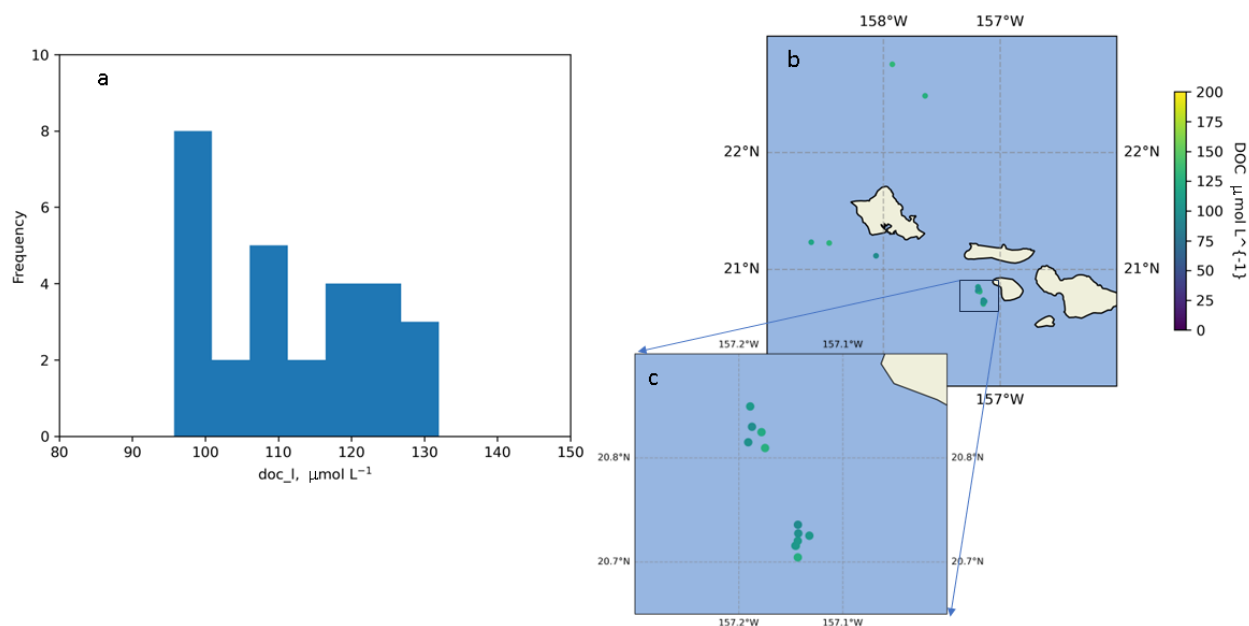
Figure 34. (a) Histogram of the concentration of dissolved organic carbon (DOC) for all samples, and (b, c) DOC for near-surface samples collected during the field campaign.

PPig samples were filtered onto 25mm GF/F filters (0.7 μm pore size) and analyzed at the NASA-GSFC HPLC analytical facility. POC samples were filtered onto 25mm GF-75 (0.3 um pore size). POC filtration was performed using a closed, in-line filter setup, where the first filter collects the sample particulates, and the additional filter downstream serves as the 'filtrate blank' (IOCCG, 2021). POC analyses were carried out at GSFC on an Elementar Vario Cube high-temperature oxidation CHNS elemental analyzer. PIC samples were filtered through 47 mm polyethylsulfone (Sartorius). Prior to storage, filters were rinsed with 3 mM borate buffer. PPig, POC, and PIC samples were wrapped in pre-combusted (450 °C, 4 h) aluminum foil pouches and stored in liquid nitrogen (LN) promptly after filtration. SPM samples were collected onto 47-mm, pre-weighed 0.2 μm pore size Nucleopore polycarbonate filters and stored at -20 °C. SPM was measured gravimetrically in a micro-balance (± 0.001 mg). Prior to weighing, samples were dried in the laboratory at 55–65°C for 2–3 days and transferred to a desiccator to reach room temperature. Samples for a_p were collected on 25mm GF-75 and stored in LN. The spectral absorption by particles will be determined in the laboratory using a benchtop spectrophotometer equipped with an integrating sphere. Samples for DOC and CDOM were filtered through 47mm GF/F filters and stored in pre-combusted dark glass 30 and 250mL glass containers, respectively. DOC samples were preserved with 80 μL of 4N HCl and stored along with the CDOM samples at 8°C.

4.7.4 Underway above-water optical measurements

Continuous underway measurements of AOPs (surface irradiance, E_s, sky radiance, L_i, water leaving radiance, L_t) were conducted from the ship's bow using a SeaBird HyperSAS radiometer array controlled by the "PySAS" Sun-tracking software and hardware package developed by the University of Maine bio-optical group. The underway above-water radiometry is continuously operating but only records data when the solar elevation is greater than 15° above the horizon. On the last day of science data collection, March 18th, the wires to the GPS were damaged. Above-water radiometry data were only collected from March 9th to March 17th.

4.7.5 In-water optical measurements

The FSG packages to measure inherent optical properties (IOPs) consisted of two separate cages. One cage had a Seabird ac-s and ac-9 (ac-9 with a 0.2 µm filter to measure a_g), a BB9, a VSF-9, a FL-3, and a CTD. The ac-s measures absorption and attenuation (and total scattering by difference) at ~80 wavelengths between 400 and 740 nm, while the ac-9 measures the same parameters at nine discrete wavelengths. The BB9 measures backscatter at nine wavelengths and 117°. The VSF-9 measures scattering at nine angles from 60° to 170° at 532 nm. The FL measures phytoplankton fluorescence at 695 nm with an excitation wavelength of 470 nm. This cage was first lowered to 10 m to purge bubbles. It was then raised to just below the sea surface and lowered down to a depth slightly deeper than the relative chlorophyll maximum. The other cage had a Sequoia Hyper-BB (HBB) and In situ Marine Optics SC-6. The HBB measures backscatter at 10 nm steps between 430 and 700 nm, which takes about 15 seconds. The SC-6 measures backscatter at six wavelengths rapidly. This smaller, second cage was lowered to around 5 m depth and held at that depth for around 10 minutes.

Apparent optical properties of both downwelling irradiance E_d and upwelling radiance L_u were measured at 24 stations using a Biospherical Instruments C-OPS system. Downwelling solar irradiance E_s was measured with a matching reference radiometer. A multi-cast method was used for deploying the radiometers. The AOP stations are shown in Table 11.

Table 11. Metadata for AOP stations of in-water radiometry with Biospherical C-OPS system aboard NOAA Ship *Oscar Elton Sette* for the VIIRS 2022 Cal/Val campaign

Station	Time (local)	Date (UTC)	Latitude (°)	Longitude (°)	Wind (kt)	Seas (ft)	Cloud cover (%)
1	1249	3/9/2022	20.81507	-157.191	5	3	30
2	1521	3/9/2022	20.80858	-157.177	11	1	30
3	1438	3/10/2022	20.70443	-157.143	8	1	30
4	1017	3/11/2022	20.71527	-157.145	3	2	10
5	1258	3/11/2022	20.82472	-157.178	11	1	50
6	1035	3/12/2022	22.75687	-157.924	15	4	10
7	1229	3/12/2022	22.48673	-157.643	15	4	80
8	1228	3/13/2022	21.22462	-158.464	13	2	10
9	1554	3/13/2022	21.2321	-158.62	2	3	20
10	1033	3/14/2022	20.72	-157.145	3	3	40
11	1214	3/14/2022	20.8494	-157.189	3	3	30
12	1534	3/14/2022	20.85577	-157.209	-	-	40
13	1033	3/15/2022	20.8275	-157.188	10	2	30
14	1229	3/15/2022			1	2	60
15	1357	3/15/2022			6	2	60
16	1642	3/15/2022	20.72522	-157.132	5	2	60
17	1149	3/16/2022			13	5	50
18	1306	3/16/2022			17	5	50
19	1642	3/16/2022	20.73092	-157.144	10	3	40
20	1024	3/17/2022			4	2	80
21	1156	3/17/2022			6	2	80
22	1513	3/17/2022	20.7274	-157.143	9	5	80
23	1649	3/17/2022			6	2	
24	1050	3/18/2022	21.11592	-158.064	4	2	10

5. An overall summary with preliminary matchup comparisons

The VIIRS ocean color science team led the seventh field campaign in the Hawaiian waters in March 2022. In situ measurements, including AOPs, IOPs, and biological and biogeochemical properties of water samples, were recovered from 24 stations. Most of the water samples were processed and analyzed after the cruise. AOPs and IOPs data were already processed preliminarily and became available for an initial assessment. All field data will eventually be submitted to NOAA STAR after quality control and used for validating and evaluating VIIRS observations. Figure 35, Figure 36, and Figure 37 present the preliminary in situ water-leaving radiance spectra measured with different instruments with coincident satellite measurements. These data include those from two profiling HyperPros and one SBA HyperPro. They are compared to the new MOBY and old MOBY measurements as well as VIIRS data onboard NPP and NOAA-20. Since spectral resolutions differ between instruments, all data were spectrally weighted according to the VIIRS spectral response function. Not all measurements are available at different stations. The two profiling HyperPros and the two MOBYs agree very well at all stations, while the SBA data trended slightly lower at blue bands. Variability was also observed between in situ measurements and the satellite data. Sources of the variability will be further examined with the final quality-assured spectra once they become available.

Figure 35. $nL_w(\lambda)$ comparisons of stations 1–8 measured during the cruise. Notations: Hyp1 – USF's HyperPro; Hyp2 – STAR's HyperPro; NPP – VIIRS/SNPP; J1 – VIIRS/NOAA-20; MN – new MOBY; MO – Old MOBY; SBA – Sky-light Blocking Apparatus. All data is from hyperspectral data spectrally weighted to the VIIRS Bands.
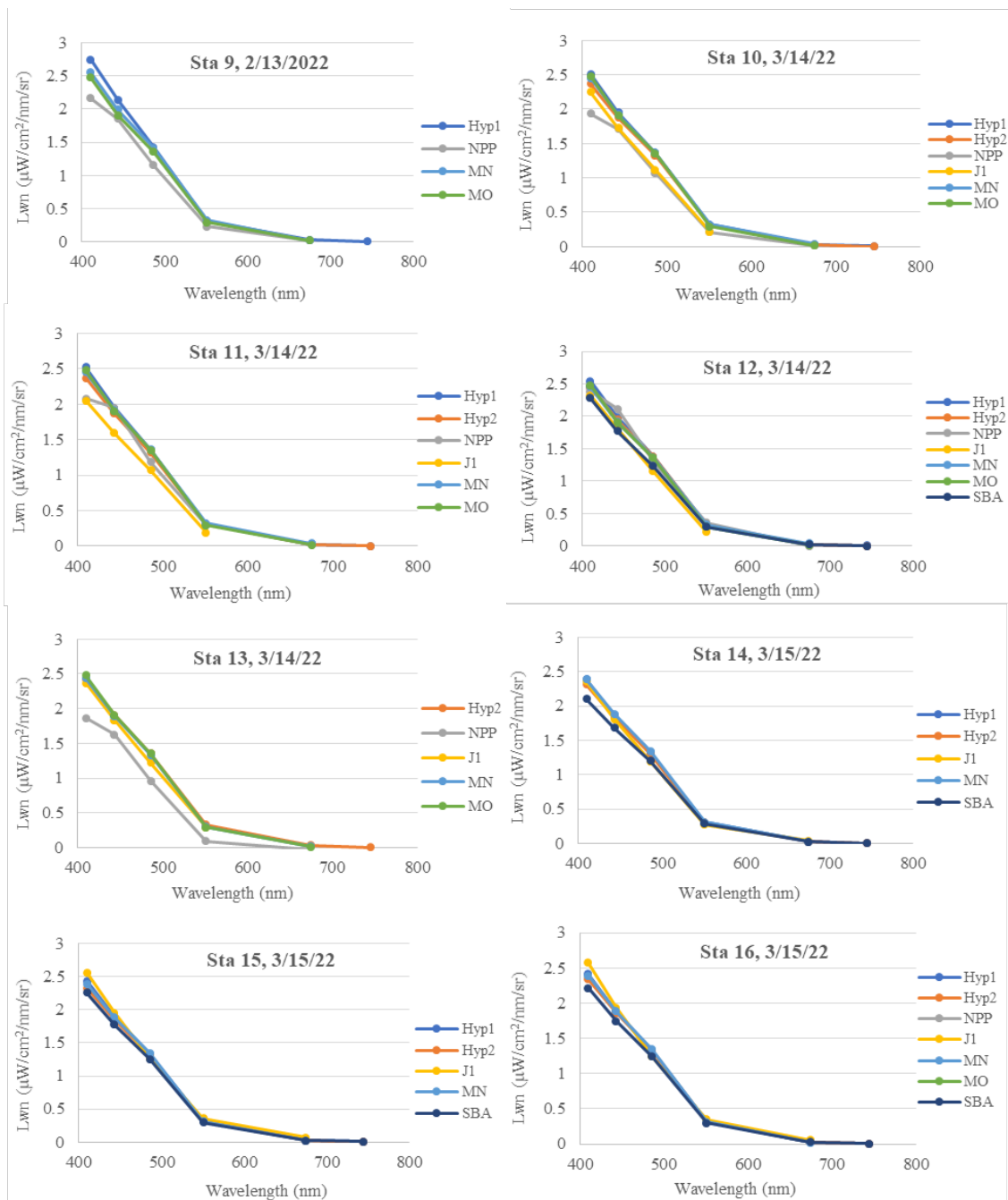
Figure 36. $nL_w(\lambda)$ comparisons of stations 9–16 measured during the cruise. Notations: Hyp1 – USF's HyperPro; Hyp2 – STAR's HyperPro; NPP – VIIRS/SNPP; J1 – VIIRS/NOAA-20; MN – new MOBY; MO – Old MOBY; SBA – Sky-light Blocking Apparatus. All data is from hyperspectral data spectrally weighted to the VIIRS Bands.
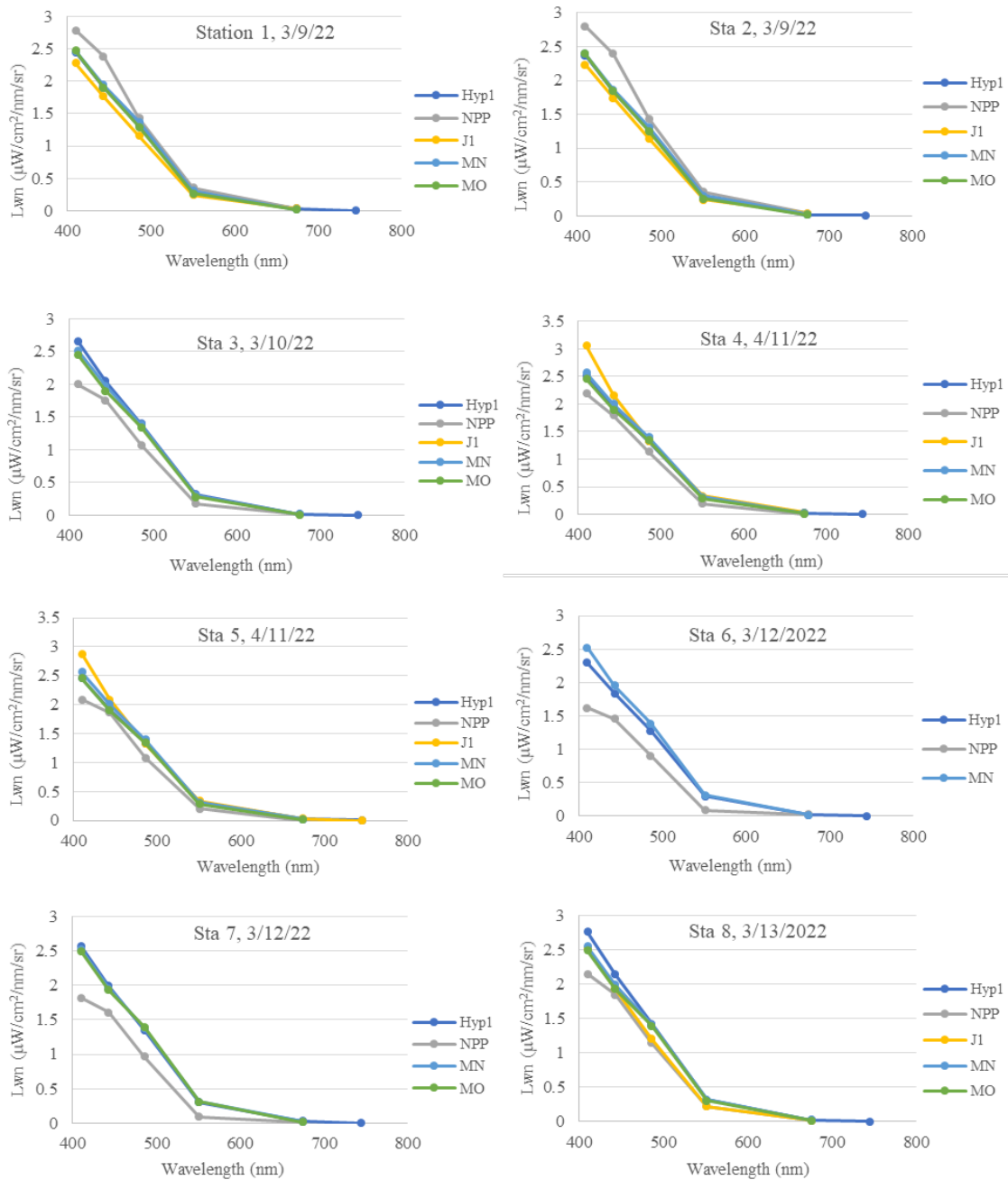
Figure 37. $nL_w(\lambda)$ comparisons of stations 17–24 measured during the cruise. Notations: Hyp1 – USF's HyperPro; Hyp2 – STAR's HyperPro; NPP – VIIRS/SNPP; J1 – VIIRS/NOAA-20; MN – new MOBY; MO – Old MOBY; SBA – Sky-light Blocking Apparatus. All data is from hyperspectral data spectrally weighted to the VIIRS Bands.
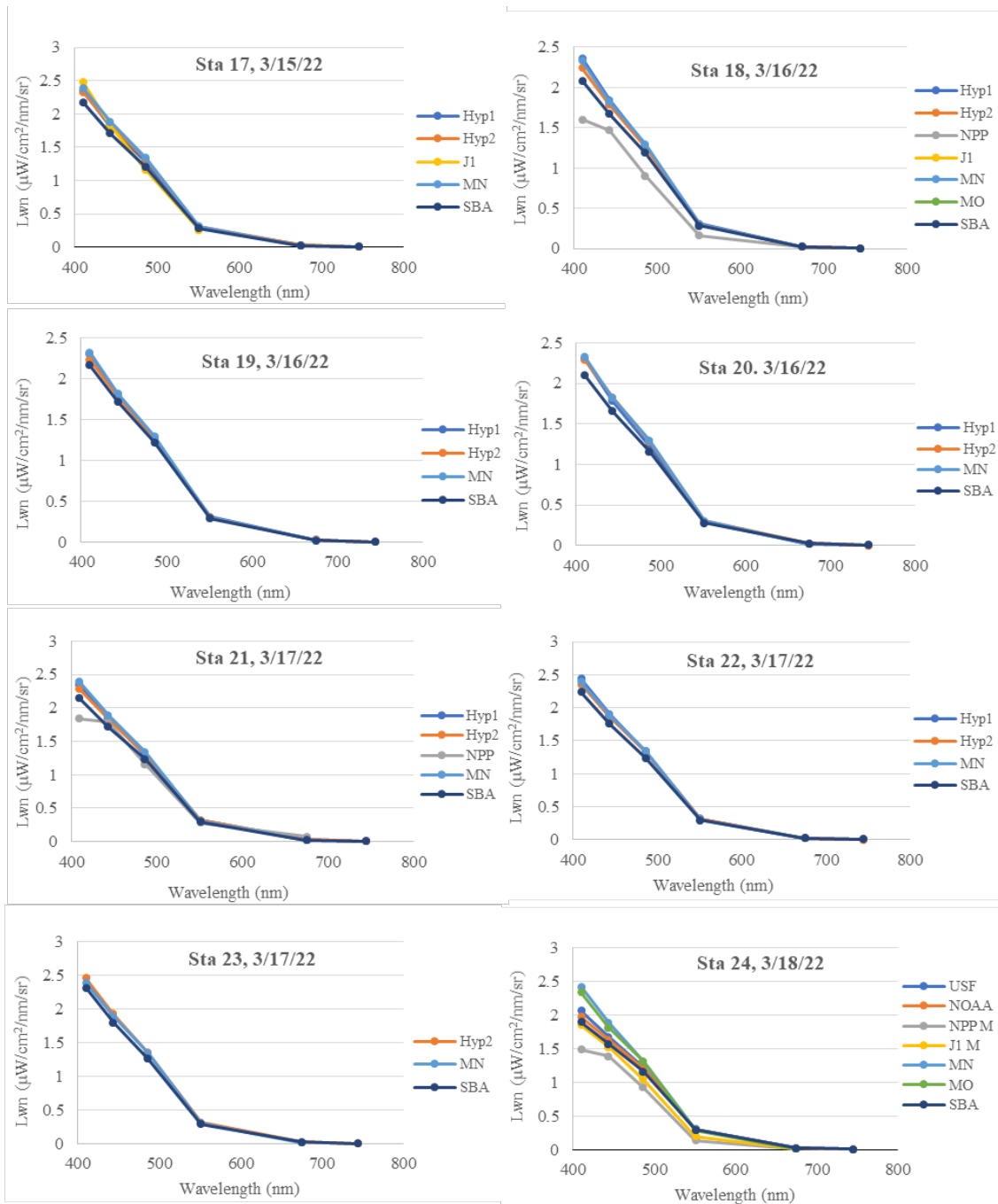
Acknowledgments

References

Barnard, A., Van Dommelen, R., Boss, E., Plache, B., Simontov, V., Orrico, C., Walter, D., Lewis, M., & Carlson, D. (2018). A new paradigm for ocean color satellite calibration and validation: accurate measurements of hyperspectral water leaving radiance from autonomous profiling floats (HYPERNAV). *ESS Open Archive,* https://doi.org/10.1002/essoar.10500047.1, 10. https://doi.org/10.1002/essoar.10500047.1

Bibby, T.S., Gorbunov, M.Y., Wyman, K.W., & Falkowski, P.G. (2008). Photosynthetic community responses to upwelling in mesoscale eddies in the subtropical North Atlantic and Pacific Oceans. *Deep Sea Research Part II: Topical Studies in Oceanography, 55*, 1310-1320. 10.1016/j.dsr2.2008.01.014

Brown, S.L., Landry, M.R., Selph, K.E., Jin Yang, E., Rii, Y.M., & Bidigare, R.R. (2008). Diatoms in the desert: Plankton community response to a mesoscale eddy in the subtropical North Pacific. *Deep Sea Research Part II: Topical Studies in Oceanography, 55*, 1321-1333. https://doi.org/10.1016/j.dsr2.2008.02.012

Calil, P.H.R., Richards, K.J., Jia, Y., & Bidigare, R.R. (2008). Eddy activity in the lee of the Hawaiian Islands. *Deep Sea Research Part II: Topical Studies in Oceanography, 55*, 1179-1194. https://doi.org/10.1016/j.dsr2.2008.01.008

Carder, K.L., & Steward, R.G. (1985). A remote-sensing reflectance model of a red tide dinoflagellate off West Florida. *Limnology and Oceanography, 30*, 286-298

Chekalyuk, A., & Hafez, M.A. (2008). Advanced laser fluorometry of natural aquatic environments. *Limnology and oceanography, methods, 6*, 591

Chekalyuk, A.M., Landry, M.R., Goericke, R., Taylor, A.G., & Hafez, M.A. (2012). Laser fluorescence analysis of phytoplankton across a frontal zone in the California Current ecosystem. *Journal of Plankton Research, 34*, 761-777. 10.1093/plankt/fbs034

Clark, D.K., Yarbrough, M.A., Feinholz, M., Flora, S., Broenkow, W., Kim, Y.S., Johnson, B.C., Brown, S.W., Yuen, M., & Mueller, J.L. (2003). MOBY, a radiometric buoy for performance monitoring and vicarious calibration of satellite ocean color sensors: measurement and data analysis protocols. In J.L. Mueller, G.S. Fargion, & G.S. McClain (Eds.), *Ocean Optics Protocols For Satellite Ocean Color Sensor Validation, Revision 4, Volume VI: Special Topics in Ocean Optics Protocols and Appendices* (pp. 138-170). Greenbelt, MD NASA, Goddard Space Flight Center

Cox, C., & Munk, W. (1954). Measurement of the roughness of the sea surface from photographs of the sun's glitter. *Journal of the Optical Society of America, 44*, 838-850

Dickey, T.D., Nencioli, F., Kuwahara, V.S., Leonard, C., Black, W., Rii, Y.M., Bidigare, R.R., & Zhang, Q. (2008). Physical and bio-optical observations of oceanic cyclones west of the island of Hawai'i. *Deep Sea Research Part II: Topical Studies in Oceanography, 55*, 1195-1217. https://doi.org/10.1016/j.dsr2.2008.01.006

Goes, J.I., Gomes, H.d.R., Chekalyuk, A.M., Carpenter, E.J., Montoya, J.P., Coles, V.J., Yager, P.L., Berelson, W.M., Capone, D.G., Foster, R.A., Steinberg, D.K., Subramaniam, A., & Hafez, M.A. (2014a). Influence of the Amazon River discharge on the biogeography of phytoplankton communities in the western tropical north Atlantic. *Progress in Oceanography, 120*, 29-40. 10.1016/j.pocean.2013.07.010

Goes, J.I., Gomes, H.d.R., Haugen, E.M., McKee, K.T., D'Sa, E.J., Chekalyuk, A.M., Stoecker, D.K., Stabeno, P.J., Saitoh, S.-I., & Sambrotto, R.N. (2014b). Fluorescence, pigment and microscopic characterization of Bering Sea phytoplankton community structure and photosynthetic competency in the presence of a Cold Pool during summer. *Deep Sea Research Part II: Topical Studies in Oceanography, 109*, 84-99. https://doi.org/10.1016/j.dsr2.2013.12.004

Gorbunov, M.Y., & Falkowski, P.G. (2004). Fluorescence induction and relaxation (FIRe) technique and instrumentation for monitoring photosynthetic processes and primary production in aquatic ecosystems. In, *Photosynthesis: Fundamental Aspects to Global Perspectives"-Proc. 13th International Congress of Photosynthesis, Montreal, Aug* (pp. 1029-1031)

Gordon, H.R., & Wang, M. (1994). Retrieval of water-leaving radiance and aerosol optical thickness over the oceans with SeaWiFS: a preliminary algorithm. *Applied Optics, 33*, 443-452

Haëntjens, N., & Boss, E. (2020). Inlinino: a modular software data logger for oceanography. *Oceanography, 33*, 80-84. https://doi.org/10.5670/oceanog.2020.112

Harmel, T., Gilerson, A., Hlaing, S., Tonizzo, A., Legbandt, T., Weidemann, A., Arnone, R., & Ahmed, S. (2011). Long Island Sound Coastal Observatory: Assessment of above-water radiometric measurement uncertainties using collocated multi and hyperspectral systems. *Applied Optics, 50*, 5842-5860. https://doi.org/10.1364/AO.50.005842

Holm-Hansen, O., & Riemann, B. (1978a). Chlorophyll a determination: improvements in methodology. *Oikos, 30*, 438-447

Holm-Hansen, O., & Riemann, E. (1978b). Chlorophyll-a determination: improvements in methodology. *Oikos, 30*, 43-47

IOCCG (2010). Atmospheric correction for remotely-sensed ocean color products. In M. Wang (Ed.) (p. 78). Dartmouth, Nova Scotia, Canada: International Ocean Color Coordinating Group

Jenkins, C., Goes, J., McKee, K., Gomes, H.d.R., Arnone, R., Wang, M., Ondrusek, M., Nagamani, P., Preethi Latha, T., Rao, K., & Dadhwal, V. (2016). High-resolution shipboard measurements of phytoplankton: a way forward for enhancing the utility of satellite SST and chlorophyll for mapping microscale features and frontal zones in coastal waters. *Proc. SPIE, 9878*. 10.1117/12.2225875

Karl, D.M., Letelier, R.M., Bidigare, R.R., Björkman, K.M., Church, M.J., Dore, J.E., & White, A.E. (2021). Seasonal-to-decadal scale variability in primary production and particulate matter export at Station ALOHA. *Progress in Oceanography, 195*, 102563. https://doi.org/10.1016/j.pocean.2021.102563

Kishino, M., Takahashi, M., Okami, N., & Ichimura, S. (1985). Estimation of the spectral absorption coefficients of phytoplankton in the sea. *Bulletin of Marine Science, 37*, 634-642

Lawson, A., Ladner, S., Crout, R., Wood, C., Arnone, R., Bowers, J., Martinolich, P., & Lewis, D. (2019). Establishing optimal matchup protocols between ocean color satellites and ground truth AeroNET-OC radiance. *Proc. SPIE, 11014*. 10.1117/12.2521062

Lee, Z.P. (2009). K_{PAR}: an optical property associated with ambiguous values. *Journal of Lake Sciences, 21*, 159-164

Lee, Z.P., Carder, K.L., & Arnone, R. (2002). Deriving inherent optical properties from water color: a multi-band quasi-analytical algorithm for optically deep waters. *Applied Optics, 41*, 5755-5772. https://doi.org/10.1364/AO.41.005755

Lee, Z.P., Wei, J., Shang, Z., Garcia, R., Dierssen, H.M., Ishizaka, J., & Castagna, A. (2019). On-water radiometry measurements: skylight-blocked approach and data processing. In G. Zibordi, K.J. Voss, B.C. Johnson, & J.L. Mueller (Eds.), *Appendix to Protocols for Satellite Ocean Colour Data Validation: In Situ Optical Radiometry. IOCCG Ocean Optics and Biogeochemistry Protocols for Satellite Ocean Colour Sensor Validation, Volume 3.0* (p. 7). Dartmouth, NS, Canada: IOCCG

Malinowski, M., Gilerson, A., Herrera-Estrella, E., & Agagliate, J. (2023). Polarimetric imaging of the ocean surface for the study of ocean surface roughness and wave slopes statistics. *Proc. SPIE, 12543*. https://doi.org/10.1117/12.2665834

Mélin, F., Zibordi, G., Berthon, J.-F., Bailey, S., Franz, B., Voss, K.J., Flora, S., & Grant, M. (2011). Assessment of MERIS reflectance data as processed with SeaDAS over the European seas. *Optics Express, 19*, 25657-25671

Mobley, C.D. (1994). *Light and water: radiative transfer in natural waters*. San Diego, California: Academic Press

Mobley, C.D. (1999). Estimation of the remote-sensing reflectance from above-surface measurements. *Applied Optics, 38*, 7442-7455

Mobley, C.D. (2015). Polarized reflectance and transmittance properties of windblown sea surfaces. *Applied Optics, 54*, 4828-4849. 10.1364/AO.54.004828

Moore, T.S., Campbell, J.W., & Dowell, M.D. (2009). A class-based approach to characterizing and mapping the uncertainty of the MODIS ocean chlorophyll product. *Remote Sensing of Environment, 113*, 2424-2430. https://doi.org/10.1016/j.rse.2009.07.016

Mueller, J., Fargion, G., & McClain, C.R. (2003a). Ocean optics protocols for satellite ocean color validation, Revision 4, Volume IV: Inherent optical properties: instruments, characterizations, field measurements and data analysis protocols. In (p. 76). Greenbelt, Maryland: NASA

Mueller, J.L., Davis, C.O., Arnone, R., Frouin, R., Carder, K., Lee, Z.P., Steward, R.G., Hooker, S.B., Mobley, C.D., & McLean, S. (2003b). Above-water radiance and remote sensing reflectance measurement and analysis protocols. In J.L. Mueller, G.S. Fargion, & C. McClain (Eds.), *Ocean Optics Protocols For Satellite Ocean Color Sensor Validation, Revison 4, Volume III: Radiometric Measurements and Data Analysis Protocols* (pp. 21 - 31). Greenbelt, Maryland: Goddard Space Flight Center, National Aeronautics and Space Administration

Nalli, N.R., Foltz, G.R., Gero, J., Gibson, L., Knuteson, R.O., Lumpkin, R., Minnett, P.J., Morris, V.R., Ondrusek, M., Perez, R.C., Wang, M., & Wei, J. (2022). Ship-based cal/val campaigns. In N.R. Nalli (Ed.), *Field measurements for passive environmental remote sensing: Instrumentation, intensive campaigns, and satellite applications* (pp. 195-217): Elsevier

Ondrusek, M., Lance, V.P., Wang, M., Arnone, R.A., Ladner, S., Goode, W., Vandermeulen, R., Freeman, S., Chaves, J.E., Mannino, A., Gilerson, A., Ahmed, S., Carrizo, C., El-Habashi, A., Foster, R., Ottaviani, M., Goes, J.I., Gomes, H.d.R., McKee, K., Hu, C., Kovach, C., English, D., Cannizzaro, J., Johnson, B.C., Lee, Z., Wei, J., Wang, Q., Lin, J., Tufillaro, N., Nahorniak, J., Davis, C.O., & Voss, K.J. (2015). Report for dedicated JPSS VIIRS Ocean Color Calibration/Validation Cruise. In V.P. Lance (Ed.), *NOAA technical report NESDIS 146* (p. 60). Washington, D.C.: NOAA National Environmental Satellite, Data, and Information Service

Ondrusek, M., Lance, V.P., Wang, M., Arnone, R.A., Ladner, S., Goode, W., Vandermeulen, R., Freeman, S., Chaves, J.E., Mannino, A., Gilerson, A., Ahmed, S., Carrizo, C., El-Habashi, A., Foster, R., Ottaviani, M., Goes, J.I., Gomes, H.d.R., McKee, K., Hu, C., Kovach, C., English, D., Cannizzaro, J., Johnson, B.C., Lee, Z., Wei, J., Wang, Q., Lin, J., Tufillaro, N., Nahorniak, J., Davis, C.O., & Voss, K.J. (2016). Report for dedicated JPSS VIIRS Ocean Color December 2015 Calibration/Validation Cruise. In V.P. Lance (Ed.), *NOAA technical report NESDIS 148* (p. 66). Silver Spring, Maryland: United States, National Environmental Satellite, Data, and Information Service

Ondrusek, M., Lance, V.P., Wang, M., Stengel, E., Kovach, C., Arnone, R.A., Ladner, S., Goode, W., Gilerson, A., Ahmed, S.A., El-Habashi, A., Foster, R., Ottaviani, M., Goes, J.I., Gomes, H.d.R., McKee, K., Kang, J.W., Hu, C., Cannizzaro, J., Sun, S., English, D., Johnson, B.C., Lee, Z., Zoffoli, L., Lin, J., Tufillaro, N., Lalovic, I., Nahorniak, J., Davis, C.O., Twardowski, M., Stockley, N., & Voss, K.J. (2017). Report for dedicated JPSS VIIRS Ocean Color Calibration/Validation Cruise, October 2016. In V.P. Lance (Ed.), *NOAA technical report NESDIS 151* (p. 65). Washington, D.C.: United States. National Environmental Satellite, Data, and Information Service

Ondrusek, M., Lance, V.P., Wang, M., Stengel, E., Kovach, C., Arnone, R.A., Ladner, S., Goode, W., Gilerson, A., El-Habashi, A., Carrizo, C., Herrera, E., Ahmed, S.A., Goes, J.I., Gomes, H.d.R., McKee, K., Hu, C., Cannizzaro, J., Zhang, Y., Huang, C.-W., English, D., Johnson, B.C., Lee, Z., Yu, X., Shang, Z., Tufillaro, N., Lalovic, I., & Voss, K.J. (2019). Report for Dedicated JPSS VIIRS Ocean Color Calibration/Validation Cruise May 2018. In V.P. Lance (Ed.), *NOAA technical report NESDIS 152* (p. 91). Washington, D.C.: United States. National Environmental Satellite, Data, and Information Service

Ondrusek, M., Lance, V.P., Wang, M., Stengel, E., Kovach, C., Freeman, S., Mannino, A., Gilerson, A., Carrizo, C., Grötsch, P., Herrera, E., Malinowski, M., Ahmed, S., Goes, J.I., Wu, J., Gomes, H.d.R., McKee, K., Hu, C., Cannizzaro, J., Zhang, Y., Zhang, Y., English, D., Ladner, S., Goode, W., Lee, Z., Wei, J., Zhang, S., Twardowski, M., Stockley, N., Strait, C., & Voss, K. (2021). Report for Dedicated JPSS VIIRS Ocean Color Calibration/Validation Cruise September 2019. In V.P. Lance

(Ed.), *NOAA Technical Report NESDIS* (p. 60). Washington D. C.: National Environmental Satellite, Data, and Information Service (NESDIS)

Ondrusek, M., Wei, J., Wang, M., Stengel, E., Kovach, C., Gilerson, A., Herrera, E., Malinowski, M., Goes, J.I., Gomes, H.d.R., McKee, K., Hu, C., Cannizzaro, J., English, D., Ladner, S., Goode, W., Tufillaro, N., & Lalovic, I. (2022). Report for dedicated JPSS VIIRS ocean color calibration/validation cruise: Gulf of Mexico in April 2021. In J. Wei (Ed.), *NOAA Technical Report NESDIS 157* (p. 51). Washington D. C., United States: NOAA National Environmental Satellite, Data Information, Service

Perez, R.C., Foltz, G.R., Lumpkin, R., Wei, J., Voss, K.J., Ondrusek, M., Wang, M., & Bourassa, M.A. (2022). Oceanographic buoys: Providing ocean data to assess the accuracy of variables derived from satellite measurements. In N.R. Nalli (Ed.), *Field Measurements for Passive Environmental Remote Sensing* (pp. 79-100): Elsevier

Pope, R.M., & Fry, E.S. (1997). Absorption spectrum (380-700 nm) of pure water. II. Integrating cavity measurements. *Applied Optics, 36*, 8710-8723

Qin, P., Simis, S.G.H., & Tilstone, G.H. (2017). Radiometric validation of atmospheric correction for MERIS in the Baltic Sea based on continuous observations from ships and AERONET-OC. *Remote Sensing of Environment, 200*, 263-280. https://doi.org/10.1016/j.rse.2017.08.024

Rii, Y.M., Brown, S.L., Nencioli, F., Kuwahara, V., Dickey, T., Karl, D.M., & Bidigare, R.R. (2008). The transient oasis: Nutrient-phytoplankton dynamics and particle export in Hawaiian lee cyclones. *Deep Sea Research Part II: Topical Studies in Oceanography, 55*, 1275-1290. https://doi.org/10.1016/j.dsr2.2008.01.013

Röttgers, R., McKee, D., & Woźniak, S.B. (2013). Evaluation of scatter corrections for ac-9 absorption measurements in coastal waters. *Methods in Oceanography, 7*, 21-39. 10.1016/j.mio.2013.11.001

Satlantic (2003). Operation Manual for Profiler II. In. Halifax, Nova Scotia: Satlantic Incorporated

Satlantic (2004). SatView Data Logging / Display Program Users Guide; Version 2.8. In. Halifax, Nova Scotia: Satlantic Incorporated

Shi, W., & Wang, M. (2019). A blended inherent optical property algorithm for global satellite ocean color observations. *Limnology and Oceanography: Methods, 17*, 377-394. https://doi.org/10.1002/lom3.10320

Wang, M. (2007). Remote sensing of the ocean contributions from ultraviolet to near-infrared using the shortwave infrared bands: simulations. *Applied Optics, 46*, 1535-1547. https://doi.org/10.1364/AO.46.001535

Wang, M., & Jiang, L. (2018). Atmospheric correction using the information from the short blue band. *IEEE Transactions on Geoscience and Remote Sensing, 56*, 6224-6237. https://doi.org/10.1109/TGRS.2018.2833839

Wang, M., Shi, W., Jiang, L., & Voss, K. (2016). NIR- and SWIR-based on-orbit vicarious calibrations for satellite ocean color sensors. *Optics Express, 24*, 20437-20453. https://doi.org/10.1364/OE.24.020437

Wang, M., Son, S., & Harding, L.W. (2009). Retrieval of diffuse attenuation coefficient in the Chesapeake Bay and turbid ocean regions for satellite ocean color applications. *Journal of Geophysical Research, 114*. 10.1029/2009JC005286

Wei, J., & Lee, Z.P. (2013). Model of the attenuation coefficient of daily photosynthetically available radiation in the upper ocean. *Methods in Oceanography, 8*, 56-74

Wei, J., Lee, Z.P., & Shang, S. (2016). A system to measure the data quality of spectral remote sensing reflectance of aquatic environments. *Journal of Geophysical Research, 121*, 8189–8207. 10.1002/2016JC012126

Wei, J., Wang, M., Jiang, L., Yu, X., Mikelsons, K., & Shen, F. (2021a). Global estimation of suspended particulate matter from satellite ocean color imagery. *Journal of Geophysical Research, 126*. https://doi.org/10.1029/2021JC017303

Wei, J., Wang, M., Lee, Z.P., Ondrusek, M., Zhang, S., & Ladner, S. (2021b). Experimental analysis of the measurement precision in spectral water-leaving radiance in different water types. *Optics Express, 29*, 2780-2797. https://doi.org/10.1364/OE.413784

Wei, J., Wang, M., Mikelsons, K., Jiang, L., Kratzer, S., Lee, Z.P., Moore, T., Sosik, H.M., & Van der Zande, D. (2022a). Global satellite water classification data products over oceanic, coastal, and inland waters. *Remote Sensing of Environment, 282*. https://doi.org/10.1016/j.rse.2022.113233

Wei, J., Wang, M., Ondrusek, M., Gilerson, A., Goes, J., Hu, C., Lee, Z., Voss, K.J., Ladner, S., Lance, V.P., & Tufillaro, N. (2022b). Satellite ocean color validation. In N. Nalli (Ed.), *Field measurements for passive environmental remote sensing: instrumentation, intensive campaigns, and satellite applications* (pp. 351-374). Cambridge, MA, United States: Elsevier

Wei, J., Yu, X., Lee, Z.P., Wang, M., & Jiang, L. (2020). Improving low-quality satellite remote sensing reflectance at blue bands over coastal and inland waters. *Remote Sensing of Environment, 250*, 112029. https://doi.org/10.1016/j.rse.2020.112029

Welschmeyer, N.A. (1994). Fluorometric analysis of chlorophyll-*a* in the presence of chlorophyll-*b* and pheopigments. *Limnology and Oceanography, 39*, 1985-1992

Werdell, P.J., Bailey, S.W., Franz, B.A., Morel, A., & McClain, C.R. (2007). On-orbit vicarious calibration of ocean color sensors using an ocean surface reflectance model. *Applied Optics, 46*, 5649-5666

Wu, J., Goes, J.I., do Rosario Gomes, H., Lee, Z., Noh, J.-H., Wei, J., Shang, Z., Salisbury, J., Mannino, A., Kim, W., Park, Y.-J., Ondrusek, M., Lance, V.P., Wang, M., & Frouin, R. (2022). Estimates of diurnal and daily net primary productivity using the Geostationary Ocean Color Imager (GOCI) data. *Remote Sensing of Environment, 280*, 113183. https://doi.org/10.1016/j.rse.2022.113183

Zappa, C.J., Banner, M.L., Schultz, H., Corrada-Emmanuel, A., Wolff, L.B., & Yalcin, J. (2008). Retrieval of short ocean wave slope using polarimetric imaging. *Measurement Science and Technology, 19*, 13pp

Zibordi, G., Mélin, F., Berthon, J.-F., Holben, B., Slutsker, I., Giles, D., D'Alimonte, D., Vandemark, D., Feng, H., Schuster, G., Fabbri, B.E., Kaitala, S., & Seppälä, J. (2009). AERONET-OC: A network for the validation of ocean color primary products. *Journal of Atmospheric and Oceanic Technology, 26*, 1634-1651. 10.1175/2009JTECHO654.1

Zibordi, G., Mélin, F., Voss, J.M., Johnson, B.C., Franz, B.A., Kwiatkowska, E.J., Huot, J.-P., Wang, M., & Antoine, D. (2015). System vicarious calibration for ocean color climate change applications: requirements for in situ data. *Remote Sensing of Environment, 159*, 361-369

Appendix: symbols, abbreviations, and acronyms

Table A 1. List of symbols and the descriptions

Symbol	Description	Units
a	(total) Light absorption coefficient	m^{-1}
a_d	Light absorption coefficient by detrital matter	m^{-1}
a_g	Light absorption coefficient by CDOM	m^{-1}
a_p	Light absorption coefficient by particles	m^{-1}
a_{pg}	Light absorption coefficient by CDOM and detritus	m^{-1}
a_{ph}	Light absorption coefficient by phytoplankton	m^{-1}
a^*_{ph}	Chlorophyll-specific phytoplankton absorption coefficient	$m^2\ mg^{-1}$
b	(total) Light scattering coefficient	m^{-1}
b_b	Backscattering coefficient of particles	m^{-1}
β	Volume scattering function (VSF)	$m^{-1}\ sr^{-1}$
β_p	Volume scattering function of particles	$m^{-1}\ sr^{-1}$
b_p	Scattering coefficient of particles	m^{-1}
c_{pg}	Total (nonwater) attenuation coefficient	m^{-1}
E_d	Downwelling irradiance	$mW\ cm^{-2}\ \mu m^{-1}$
E_s	Downwelling irradiance just above water surface	$mW\ cm^{-2}\ \mu m^{-1}$
K_d	Diffuse attenuation coefficient for downwelling irradiance	m^{-1}
L_{surf}	Total radiance from water surface	$mW\ cm^{-2}\ \mu m^{-1}\ sr^{-1}$
L_{sky}	Radiance of sky	$mW\ cm^{-2}\ \mu m^{-1}\ sr^{-1}$
L_u	Upwelling radiance	$mW\ cm^{-2}\ \mu m^{-1}\ sr^{-1}$
$L_u(0^-, \lambda)$	Spectral upwelling radiance just below water surface	$mW\ cm^{-2}\ \mu m^{-1}\ sr^{-1}$
L_w	Water-leaving radiance	$mW\ cm^{-2}\ \mu m^{-1}\ sr^{-1}$
nL_w	Normalized water-leaving radiance	$mW\ cm^{-2}\ \mu m^{-1}\ sr^{-1}$
R_{rs}	Remote sensing reflectance	sr^{-1}
w	Wind speed	m/s
λ	Wavelength	nm
φ	Relative azimuth of the sensor to the sun	deg
ρ	Fresnel reflectance factor of seawater	
θ	Zenith Angle	deg

Table A 2. List of abbreviations and acronyms (excluding instruments)

Name	Description
AC	Atmospheric correction
AERONET-OC	Aerosol Robotic Network-Ocean Color
AoLP	Angle of Linear Polarization
AOP	Apparent optical property
AOT	Aerosol optical thickness
BRDF	Bidirectional reflectance distribution function
Cal/Val	Calibration and Validation
CCNY	City College of New York
CDOM	Chromophoric dissolved organic material
Chl-a	Chlorophyll-a concentration
DoLP	Degree of linear polarization
EDR	Environmental Data Record
FOV	Field of view
FWHM	Full width at half maximum
GCOM-C	Global Climate Observation Mission-Climate
GPS	Global Positioning System
GSFC	Goddard Space Flight Center
HEPA	High efficiency particulate absorbing
HOT	Hawaii Ocean Time-series
HPLC	High Pressure Liquid Chromatography
IFOV	Instantaneous field of view
IOP	Inherent optical property
JPSS	Joint Polar Satellite System (program)
LDEO	Lamont-Doherty Earth Observatory at Columbia University
MOBY	Marine Optical BuoY
MSL12	Multi-Sensor Level-1 to Level-2

Table A 3. Continuation of Table A2

Name	Description
NASA	National Aeronautics and Space Administration
NCEI	National Centers for Environmental Information
NESDIS	National Environmental Satellite, Data, and Information Service
NIR	Near-infrared
NIST	National Institute of Standards and Technology
NRL	Naval Research Laboratory
NOAA	National Oceanic and Atmospheric Administration
NPSG	North Pacific Subtropical Gyre
OC	Ocean Color
OCI	Ocean Color Irradiance
OCR	Ocean Colour Radiance
OLCI	Ocean and Land Colour Instrument
OMAO	Office of Marine and Air Operations
OSU	Oregon State University
PAR	Photosynthetically available radiation (400–700 nm)
PFT	Phytoplankton Functional Type
QAA	Quasi-analytical algorithm
SBA	Skylight-blocking apparatus
SGLI	Second Generation Global Imager
SNPP	Suomi National Polar-orbiting Partnership
SPM	Suspended Particulate Matter
SST	Sea surface temperature
STAR	Center for Satellite Applications and Research
SWIR	Shortwave infrared
UMB	University of Massachusetts Boston
USF	University of South Florida
UV	Ultraviolet
VIIRS	Visible Infrared Imaging Radiometer Suite

Table A 4. List of instrument abbreviations and acronyms

Name	Description	Manufacturer
ac-9	Absorption and attenuation meter (9 bands)	WET Labs; Sea-Bird Scientific
ac-s	Absorption and attenuation meter (hyperspectral)	WET Labs; Sea-Bird Scientific
ALF	Automated Laser Fluorometer	
ASD	Analytical spectral device	PANalytical
BB3	Backscattering sensor (3 bands)	WET Labs; Sea-Bird Scientific
BB9	Backscattering sensor (9 bands)	WET Labs; Sea-Bird Scientific
C-OPS	Compact optical profiling system	Biospherical Instruments Inc.
CTD	Conductivity, temperature, depth	Generic, various manufacturers
FIRe	Variable fluorescence	Satlantic, now Sea-Bird
FlowCam	Dynamic imaging particle analysis for species composition and size measurements	Fluid Imaging Technologies, Inc.
GER	Field portable spectroradiometer	Spectra Vista Corporation
HyperNAV	Hyperspectral autonomous profiling float	Sea-Bird
HyperOCI	Hyperspectral irradiance sensor	Satlantic, now Sea-Bird
HyperOCR	Hyperspectral radiance sensor	Satlantic, now Sea-Bird
HyperProI, HyperPro-II	Free-falling hyperspectral optical profiler	Satlantic, now Sea-Bird
HyperSAS	Hyperspectral surface acquisition system	Satlantic, now Sea-Bird
Microtops	Handheld sun photometer	Solar Light Company
SEI	Spectral Evolution hyperspectral spectroradiometer	Spectral Evolution